ELSEVIER

Journal of Molecular Catalysis A: Chemical 112 (1996) 167–194

JOURNAL OF MOLECULAR CATALYSIS A: CHEMICAL

Charge response study of the toluene–$[V_2O_5]$ chemisorption clusters: Two reactant approach

Roman F. Nalewajski *, J. Korchowiec

K. Gumiński Department of Theoretical Chemistry, Jagiellonian University, R. Ingardena 3, 30-060 Cracow, Poland

Received 27 September 1995; accepted 29 February 1996

Abstract

Using the charge sensitivity analysis in the atomic resolution the shifts in electron populations of constituent atoms due to the intra-reactant polarization (P), inter-reactant charge transfer (CT), and the resulting overall (P + CT) patterns, are compared for alternative perpendicular and parallel chemisorption systems including toluene and the two (010)-layer, nearly stoichiometric $V_{36}O_{98}$ cluster. At each level of description a relative role of the diagonal (intra-reactant) and off-diagonal (inter-reactant) terms is examined. These isoelectronic (in situ) diagrams are supplemented by the global Fukui function diagrams, characterizing the open chemisorption system as a whole, in contact with the external electron reservoir. The in situ charge reconstruction patterns are predicted to be strongly localized in the chemisorption region, while the global Fukui function diagrams are delocalized throughout the whole cluster. In most cases the total isoelectronic responses are dominated by the diagonal contributions of the adsorbate and the off-diagonal component of the surface cluster. The in situ reactivity information is used to probe the adsorbate activation patterns and surface reconstruction trends for the eight most important (perpendicular and parallel) molecular chemisorption arrangements. The external CT data similarly reflect upon changes in the electronic/bond structure induced by the inflow/outflow of electrons to/from the chemisorption system, thus providing a qualitative information about the influence of the CT involving the cluster environment upon the chemisorption complex.

1. Introduction

The molecular charge sensitivity analysis (CSA) in the atoms-in-molecules (AIM) resolution [1–5] represents a systematic procedure for determining chemically interesting charge responses, to be used in diagnosing trends in chemical reactivity of very large systems, from the model AIM hardness matrix (see the Appendix): $\eta = \partial^2 E/\partial \mathbf{N}\,\partial \mathbf{N} = \partial \mathbf{u}/\partial \mathbf{N} \cong \{\gamma_{i,j}\}$; here E is the system electronic energy, $\mathbf{N} = \{N_i\}$ is the row vector of the AIM electron populations, $\mathbf{u} = \{\mu_i\}$ stands for the row vector of the AIM chemical potentials, $\mathbf{u} = \partial E/\partial \mathbf{N}$, and $\{\gamma_{i,j}\}$ are the valence-shell electron repulsion integrals estimated, e.g., from the familiar Pariser/Ohno [6] interpolation formulas of the semi-empirical SCF MO theories. The CSA is based upon the phenomenological AIM discretization of the fundamental Euler (electronegativity equaliza-

* Corresponding author.

PII S1381-1169(96)00130-6

tion) equations of the density functional theory (DFT) [7–9].

In the theory of chemical reactivity one usually views the overall pattern of the electronic charge reconstruction in the reactive system, M = A–B, relative to that in the separated reactants, $M^0 = A + B$, as resulting from the reactants mutual polarization (P) and the inter-reactant charge transfer (CT). The polarization stage is conventionally treated as creating conditions for the final CT between reactants. The polarized reactants in $M^{(+)} = (A^+|B^+)$ exhibit the intra-reactant electronegativity equalization, before the final inter-reactant CT, which equalizes the electronegativity throughout the whole $M^{(*)} = (A^*|B^*)$ (see the Appendix). The charge response diagrams for all these levels of description can be quickly generated within the CSA in a truly two-reactant approach, which takes into account the reactant interaction. These in situ responses are isoelectronic in character since they preserve the overall number of electrons in the reactive system: $N = N_A + N_B =$ const. In the heterogeneous catalysis of interest also are the open-system (global) characteristics of M, describing the effect of the external charge transfer, $dN \neq 0$, between M and the external electron reservoir, e.g., surface support, the cluster environment in the crystal, etc. The absolute AIM charge displacements are the products of perturbations and the second-order response properties of reactants. The perturbations of interest in the theory of chemical reactivity are displacements in the external potentials on constituent AIM, due to the presence of the other reactant, dv, and the amount of inter-reactant CT.

$$\mathcal{N} = dN_A = -dN_B > 0, \tag{1}$$

where A and B denote the acidic and basic reactants in M, respectively. The dv perturbation can be approximated using the point charge approach (we assume that the AIM charge distribution of the separated reactants is available); the $d\mathcal{N}$ displacement then follows from the global electronegativity equalization (see Appendix). The P-changes in the AIM electron populations, relative to the separated reactant values, $d\mathbf{N}^{(+)}$, are due to dv alone ($\mathcal{N} = 0$), $d\mathbf{N}^{(+)} = d\mathbf{N}^{(+)}[d\mathbf{v}]_{\mathcal{N}=0}$, while the CT displacements $d\mathbf{N}^{(*)}$, relative to the polarized reactants, describe the final stage of the charge reconstruction, due to $\mathcal{N}$ alone: $d\mathbf{N}^{(*)} = d\mathbf{N}^{(*)}[\mathcal{N}]_{\mathbf{v}^0+d\mathbf{v}}$; their sum generates the overall (P + CT) shifts in the AIM populations:

$$d\mathbf{N} = d\mathbf{N}[d\mathbf{v}, \mathcal{N}] = d\mathbf{N}^{(+)} + d\mathbf{N}^{(*)}. \tag{2}$$

Typical CT reactivity criteria are formulated in terms of the Fukui function indices (FFI) [8], representing the AIM charge reorganizations per unit external or internal CT. Most of the calculations reported in the literature are based upon the single-reactant approach, neglecting the influence of one reactant upon another in the actual reactive system; this perspective may be inadequate when large reactants are involved [2,3,5]. The reactant mutual influence is explicitly taken into account in the recently proposed two-reactant treatment of charge responses [2,3,5], which takes into account both the diagonal (intra-reactant) and off-diagonal (inter-reactant) P and CT contributions. The isoelectronic CT responses of the interacting species have been shown to represent very sensitive reactivity criteria, only weakly dependent upon the adopted cluster approximation [2,5]. These in situ responses are usually strongly localized in the region of chemisorption bond(s) so that much smaller surface clusters are needed to obtain convergent results.

Previous CSA [10–12], SCF MO and DFT studies [13–15] of the vanadium toluene chemisorption systems have usually adopted a very small, strongly nonstoichiometric cluster representation of the surface active site, including a few idealized VO_5 pyramids of the surface layer, and the single-reactant approach. As shown in the recent study [14] the cluster size and stoichiometry have rather strong effect upon the global FFI, characterizing the system as a whole, thus affecting the reactivity predictions

based upon this criterion. Moreover, no attempt to include the P-component has been made in previous CSA calculations; these polarizational charge displacements may also alter in some cases predictions of the reactivity trends from the CT pattern alone. Such complete CSA analysis will be presented in this article for the first time.

It is the main purpose of the present work to calculate the P, CT, and overall (P + CT) in situ AIM charge response diagrams, as well as the corresponding global FF patterns for chemisorption systems involving large, two (010)-layer, nearly-stoichiometric cluster V_{36} O_{98} [14] modelling the vanadium pentoxide surface, and the molecularly adsorbed toluene. The CSA calculations will be carried out using the consistent two-reactant approach taking into account the reactant interaction and both the $d\mathbf{v}$ and $\mathcal{N}$ perturbations. The crystallographic angles [16] are used with the optimized bond lengths in each layer; also the crystallographic value of the inter-layer V–O bond length have been assumed. The eight most important arrangements of the molecularly adsorbed toluene are examined, five exhibiting perpendicular orientation of the benzene ring relative to the surface (adsorption of the methyl fragment) and three parallel arrangements of the benzene ring on the surface. The relative role of the intra-reactant (diagonal) and inter-reactant (off-diagonal) responses on both reactants is investigated and the influence of the supporting layer, moderating the charge displacements due to the chemisorption on the surface layer, is examined. The response criteria are used to predict the activation patterns of toluene and the surface relaxation effects for all alternative chemisorption structures. It is also the goal of this study to identify specific effects due to changes in the mutual geometrical arrangement of the toluene and the surface cluster, and to compare the charge reconstruction patterns at the above three levels of describing the isoelectronic processes, to see whether the CT-induced charge shifts in the reaction region enhance/diminish the direct polarizational displacements. The global (external) CT information will be used to predict the environmental CT effects upon the chemisorption/desorption processes. These findings are compared with conclusions drawn from the previous CSA and SCF MO results.

2. Charge response properties

In this short outline of the charge responses which we use in the present analysis to probe reactivity trends of the toluene–$[V_2O_5]$ system, we shall often refer to the Appendix, where some intermediate quantities are defined and the algorithms for calculating them from the canonical AIM hardness matrix are described.

2.1. Mutual polarization of reactants

The perturbing external potential $d\mathbf{v}$ (Eq. (A.3)), due to the presence of the other reactant in M = (A|B), generates differences in the AIM chemical potentials $\mathbf{u}_X^{(+)} = \mathbf{u}_X^0 + d\mathbf{v}_X$ of the reactants X = A, B, when the separated reactant AIM charges are held 'frozen' in M. The first-order polarizational charge reconstruction of the mutually closed reactants, which equalizes the chemical potentials (electronegativities) of all AIM in a single reactant, can be calculated from the linear response matrix of Eq. (A.7):

$$d\mathbf{N}^{(+)} = \left[d\mathbf{N}_A^{(+)}, d\mathbf{N}_B^{(+)}\right]; \tag{3a}$$

$$\begin{aligned} d\mathbf{N}_A^{(+)} &= \left[d\mathbf{v}_A(\partial \mathbf{N}_A/\partial \mathbf{v}_A)_{N_A,N_B,v_B}\right] \\ &\quad + \left[d\mathbf{v}_B(\partial \mathbf{N}_A/\partial \mathbf{v}_B)_{N_A,N_B,v_A}\right] \\ &= \left[d\mathbf{v}_A\,\boldsymbol{\beta}^{A,A}\right] + \left[d\mathbf{v}_B\,\boldsymbol{\beta}^{B,A}\right] \\ &\equiv \left[d\mathbf{N}_A^{(+)}(\text{diagonal})\right] \\ &\quad + \left[d\mathbf{N}_A^{(+)}(\text{off-diagonal})\right], \text{ etc.} \end{aligned} \tag{3b}$$

The overall diagonal and off-diagonal components are obtained by combining the respective reactant vectors: $d\mathbf{N}^{(+)}(\text{diagonal}) = [d\mathbf{N}_A^{(+)}(\text{diagonal}),\ d\mathbf{N}_B^{(+)}(\text{diagonal})]$, and

$d\mathbf{N}^{(+)}$(off-diagonal) = [$d\mathbf{N}_A^{(+)}$(off-diagonal), $d\mathbf{N}_B^{(+)}$(off-diagonal)].

2.2. *Fukui function indices and the in situ CT populational displacements*

The global FFI (Eq. (A.9)), $\mathbf{f} = (\partial\mathbf{N}/\partial N)_v$, where $\mathbf{N} = \{N_i\} = (\mathbf{N}_A, \mathbf{N}_B)$ groups atomic electron populations of both reactants and N is the global number of electrons, provide the charge reorganization pattern due to the inflow of a single electron, $dN = 1$, from a hypothetical electron reservoir. They refer to the global equilibrium in the whole $M = (A^{(*)}|B^{(*)})$ (mutually opened reactants, see Appendix) and do not provide a link between properties of the separated reactants, their interaction, and the resulting inter-reactant (internal) CT. However, they can be used to diagnose the effect of an external CT involving the system environment represented by the hypothetical reservoir in of the combined system: (A|B|*reservoir*).

Consider now various FF quantities for the M = (A|B) partitioning, which can be used to calculate the isoelectronic (in situ) indices corresponding to the single B → A electron transfer (Eq. (1)).

The rigid (diagonal) reactant AIM FFI, $\tilde{\mathbf{f}}^{X,X} \equiv (\partial\mathbf{N}_X/\partial N_X)_{N_Y,v}$, where we have indicated the assumed 'frozen' AIM populations of the other reactant, are calculated via separately inverting the diagonal blocks $\eta^{X,X}$ of η. The $\{\tilde{\mathbf{f}}^{X,X}\}$ totally neglect the inter-reactant charge coupling in M = A–B, represented by the off-diagonal blocks of the hardness matrix, $\eta^{X,Y}$, $X \neq Y$. All diagonal FFI must be normalized to a single electron, e.g., $\sum_x^X \tilde{f}_x^{X,X} = (\partial N_X/\partial N_X)_{N_Y,v} = 1$, where $x \in X$.

In yet another hypothetical system M = (*reservoir*$_A$|A|B|*reservoir*$_B$), where both reactants are mutually closed but allowed to separately exchange electrons with their respective reservoirs, one defines the corresponding (relaxed) diagonal FFI, $\mathbf{f}^{X,X} = (\partial\mathbf{N}_X/\partial N_X)_{N_Y,v}$, and the (relaxed) off-diagonal FFI, $\mathbf{f}^{Y,X} = (\partial\mathbf{N}_X/\partial N_Y)_{N_X,v}$ (Eq. (A.6)), with the latter summing up to zero: $\sum_x^X f_x^{Y,X} = (\partial N_X/\partial N_Y)_{N_X} = 0$. These quantities result from the matrix Eq. (A.4), which takes into account the full reactant charge coupling.

The corresponding in situ FFI, $\mathbf{f}^{\mathcal{N}} = [(\partial\mathbf{N}_A/\partial\mathcal{N})_{N,v}, (\partial\mathbf{N}_B/\partial\mathcal{N})_{N,v}]$ can be calculated from the relevant reactant quantities via the following chain rule transformations, which include the implicit dependences between global electron populations of reactants in the isoelectronic process of Eq. (1) [17]:

$$\begin{aligned}\partial\mathbf{N}_A/\partial\mathcal{N} &= (\partial\mathbf{N}_A/\partial N_A)(\partial N_A/\partial\mathcal{N}) \\ &\quad + (\partial\mathbf{N}_A/\partial N_B)(\partial N_B/\partial\mathcal{N}) \\ &= \mathbf{f}^{A,A} - \mathbf{f}^{B,A} \equiv \mathbf{f}_A^{\mathcal{N}}, \\ \partial\mathbf{N}_B/\partial\mathcal{N} &= (\partial\mathbf{N}_B/\partial N_A)(\partial N_A/\partial\mathcal{N}) \\ &\quad + (\partial\mathbf{N}_B/\partial N_B)(\partial N_B/\partial\mathcal{N}) \\ &= \mathbf{f}^{A,B} - \mathbf{f}^{B,B} \equiv -\mathbf{f}_B^{\mathcal{N}}. \end{aligned} \tag{4}$$

The charge displacement vector $\mathbf{f}^{\mathcal{N}}$ includes both the diagonal and off-diagonal contributions:

$$\begin{aligned}\mathbf{f}^{\mathcal{N}} &= (\mathbf{f}^{A,A}, -\mathbf{f}^{B,B}) + (-\mathbf{f}^{B,A}, \mathbf{f}^{A,B}) \\ &\equiv \mathbf{f}^{\mathcal{N}}(\text{diagonal}) + \mathbf{f}^{\mathcal{N}}(\text{off-diagonal}),\end{aligned} \tag{5}$$

which can be examined separately to determine their relative role in chemisorption processes.

The isoelectronic FFI provide only the relative pattern of the AIM charge displacements, normalized to the single electron transfer. Also the signs of these displacements depend upon the identity of the acidic (A) and basic (B) reactants in M, which cannot be a priori specified in a general system of strongly interacting subsystems. In the CSA framework both the amount of the internal CT and the acidic/basic character of reactants can be easily ascertained from the levels of equilibrium chemical potentials $\mu_A^{(+)} < \mu_B^{(+)}$, and the condensed hardnesses of Eq. (A.4):

$$\begin{aligned}\mathcal{N} &= -\left(\mu_A^{(+)} - \mu_B^{(+)}\right)/(\eta_{A,A} + \eta_{B,B} - 2\eta_{A,B}) \\ &\equiv -\mu_{CT}^{(+)}/\eta_{CT}^{(+)}.\end{aligned} \tag{6}$$

This information allows one to determine the

first-order CT induced displacements in the AIM electron populations:

$$\begin{aligned} d\mathbf{N}^{(*)} &= \mathscr{N}\mathbf{f}^{\mathscr{N}}, \\ d\mathbf{N}^{(*)}(\text{diagonal}) &= \mathscr{N}\mathbf{f}^{\mathscr{N}}(\text{diagonal}), \\ dN^{(*)}(\text{off-diagonal}) &= \mathscr{N}\mathbf{f}^{\mathscr{N}}(\text{off-diagonal}). \end{aligned} \tag{7}$$

The populational shifts of Eqs. (3) and (7) determine the overall pattern of Eq. (2) and its resolution:

$$\begin{aligned} d\mathbf{N}(\text{diagonal}) &= d\mathbf{N}^{(*)}(\text{diagonal}) \\ &\quad + d\mathbf{N}^{(+)}(\text{diagonal}), \\ d\mathbf{N}(\text{off-diagonal}) &= d\mathbf{N}^{(*)}(\text{off-diagonal}) \\ &\quad + d\mathbf{N}^{(+)}(\text{off-diagonal}). \end{aligned} \tag{8}$$

The algorithm for calculating all the above response properties from the AIM hardness tensor of the A–B system has been described elsewhere [1–3,18] and is summarized in the Appendix.

We conclude this short theoretical outline with a few remarks upon the CSA estimates of the approximate electrostatic (E_{ES}), polarization (E_P) and charge transfer (E_{CT}) interaction energies. The relevant expressions are [3] (see Appendix):

$$\begin{aligned} E_{ES} &\cong \sum_{a}^{A}\sum_{b}^{B} q_a q_b / |\vec{R}_a - \vec{R}_b|, \\ E_P &= \tfrac{1}{2} d\mathbf{v}\, \beta^{(A|B)} d\mathbf{v}^{\dagger}, \\ E_{CT} &\cong -\left(\mu_{CT}^{(+)}\right)^2 / \left(2\eta_{CT}^{(+)}\right). \end{aligned} \tag{9}$$

These rough energy estimates can be used to quickly generate an approximate energetical hierarchies (overall and at different reaction stages) of the compared chemisorption structures. This provides a supplementary guiding tool in cases, where independent rigorous results on small systems are not available. It should be observed, that the electrostatic energy can be either positive or negative, while the polarizational energy must always lower the system energy, as resulting from the spontaneous adjustments of the system charge distribution to the displaced external potentials of reactants. The CT energy has to be negative for internally stable polarized reactants before CT, $\eta_{CT}^{(+)} > 0$, and positive for internally unstable systems, $\eta_{CT}^{(+)} < 0$. The sum $E \equiv E_{ES} + E_P + E_{CT}$ defines the total interaction energy in the CSA approximation.

3. Results

In Fig. 1 we present a perspective view of an idealized vanadium pentoxide (010)-surface (panel a), with the regular VO_5 square pyramidal units, and the two views of the representative two-layer, nearly stoichiometric cluster $V_{36}O_{98}$ of the real crystal, which is used in the present study: on the top (panel b) and bottom (panel c) layers, respectively. The corresponding elements of these top and bottom 'surfaces' model alternative active-sites for the toluene adsorption [13]; they are specified in Fig. 2. The other layer, not involved directly in the chemisorption bond(s), models the surface 'support' in the crystal. The chemisorption systems in Fig. 2(a–e) represent prototype perpendicular adsorptions of toluene, via the methyl group, on various oxygen sites and the vanadium atom: on the terminal, singly-coordinated (vanadyl) oxygen, $O_{(1)}$, of the top layer surface (panel a), on the bridging, doubly-coordinated oxygens, $O_{(2)}$, of the bottom (panel b) and top (panel c) layer surfaces, on the triply coordinated oxygen, $O_{(3)}$, of the bottom layer surface (panel d), and on the vanadium site of the bottom layer surface (panel e). For all perpendicular chemisorption structures another toluene conformation, involving the 90° rotation of the toluene ring with respect to the methyl group, around the C–CH_3 bond, has also been examined. However, since practically no influence of this internal rotation on the predicted responses has been found we report results for one rotamer only.

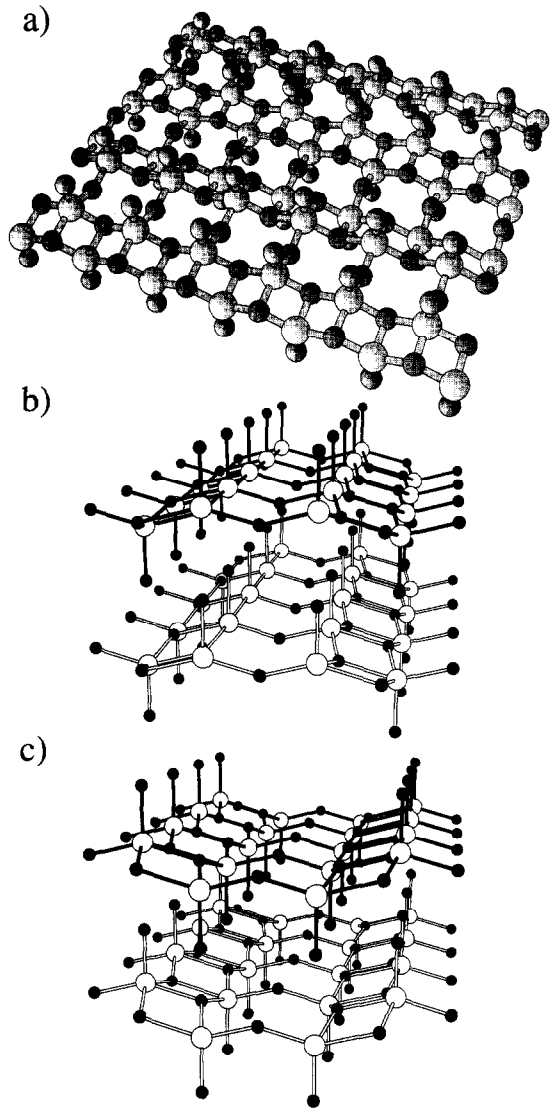

Fig. 1. Perspective views of an idealized (010)-surface of the vanadium pentoxide, involving the regular VO_5 square pyramidal units (panel a), and of a model representation the 'real' crystal surface by the nearly-stoichiometric, two-layer surface cluster $V_{36}O_{98}$: from the top layer side (panel b) and from the bottom layer side (panel c).

Fig. 2(f–h) correspond to the alternative parallel adsorption arrangements of the toluene benzene ring relative to the bottom layer surface. The first parallel complex (Fig. 2f) corresponds to the central position of the benzene ring above the vanadium (positive electrostatic potential [12]) site, which should stabilize the ring π-electrons. The second parallel adsorption arrangement (Fig. 2g) places the ring center above the central $O_{(2)}$ atom; this brings the hydrogen atoms close to the four $O_{(3)}$ sites on the surface, and the ring electrons are located close to the two vanadium atoms. However, in this test structure hydrogens are also placed close to the vanadium atoms, which should give rise to a repulsive electrostatic interaction. Finally, in the third parallel complex (Fig. 2h) the ring is above the 'cage' defined by the four vanadium atoms connected through the pairs of the $O_{(2)}$ and $O_{(3)}$ bridges.

The remaining figures report the charge response patterns for the adsorption arrangements of Fig. 2. In Figs. 3 and 4 we present the resolution of the P ($d\mathbf{N}^{(+)}$), CT ($d\mathbf{N}^{(*)}$), and overall ($d\mathbf{N}$) responses into the corresponding diagonal and off-diagonal contributions, for the illustrative perpendicular and parallel adsorptions, respectively. The total responses at the P, CT and (P + CT) levels for all structures are compared in Figs. 5 and 6. The arrow in the total CT diagrams shows the CSA determined direction of the interreactant CT. Finally, in Figs. 7 and 8 the global FFI are reported.

In Fig. 5(c, d), Fig. 6((a, b), (c, d), (e, f)), Fig. 7(c, d), and Fig. 8((a, b), (c, d), (e, f)), two representative adsorbate–substrate distances are used, with the first panel in the parentheses corresponding to the shorter distance used previously [13], and the second panel representing an earlier stage of the adsorbate approach, with the corresponding inter-reactant distance increased by 1 Å relative to the first one. We have also carried out the CSA calculations for the increased (by 1 Å) inter-reactant distance for the remaining perpendicular complexes of Fig. 2(a, b, d, e), although no charge reconstruction diagrams will be explicitly reported for these geometries. However, we shall also discuss some qualitative energetical and the CT direction results for these early approach structures.

In order to clearly see the reaction of the supporting layer to an adsorption on the surface layer, we have artificially separated the two

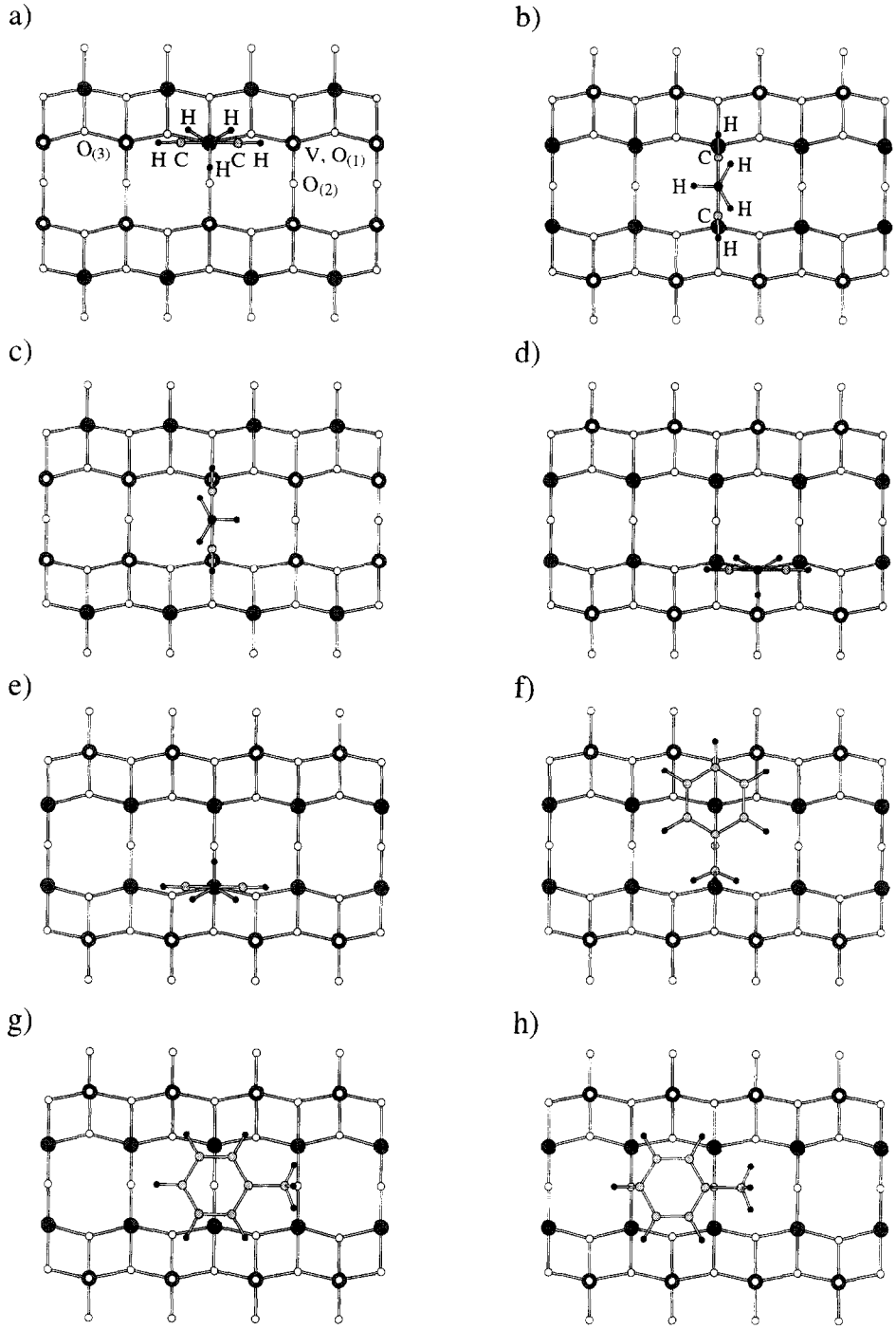

Fig. 2. The top (a, c) and bottom (b, d–h) layer views of alternative perpendicular (a–e) and parallel (f–h) adsorptions of toluene: on the vanadyl oxygen $O_{(1)}$ (a), on the bridging oxygen $O_{(2)}$ from the bottom layer side (b) and from the top layer side (c), on the triply coordinated oxygen $O_{(3)}$ (d), on the vanadium atom of the bottom layer (e), and the three parallel adsorptions of the toluene benzene ring on the bottom layer surface (f–h).

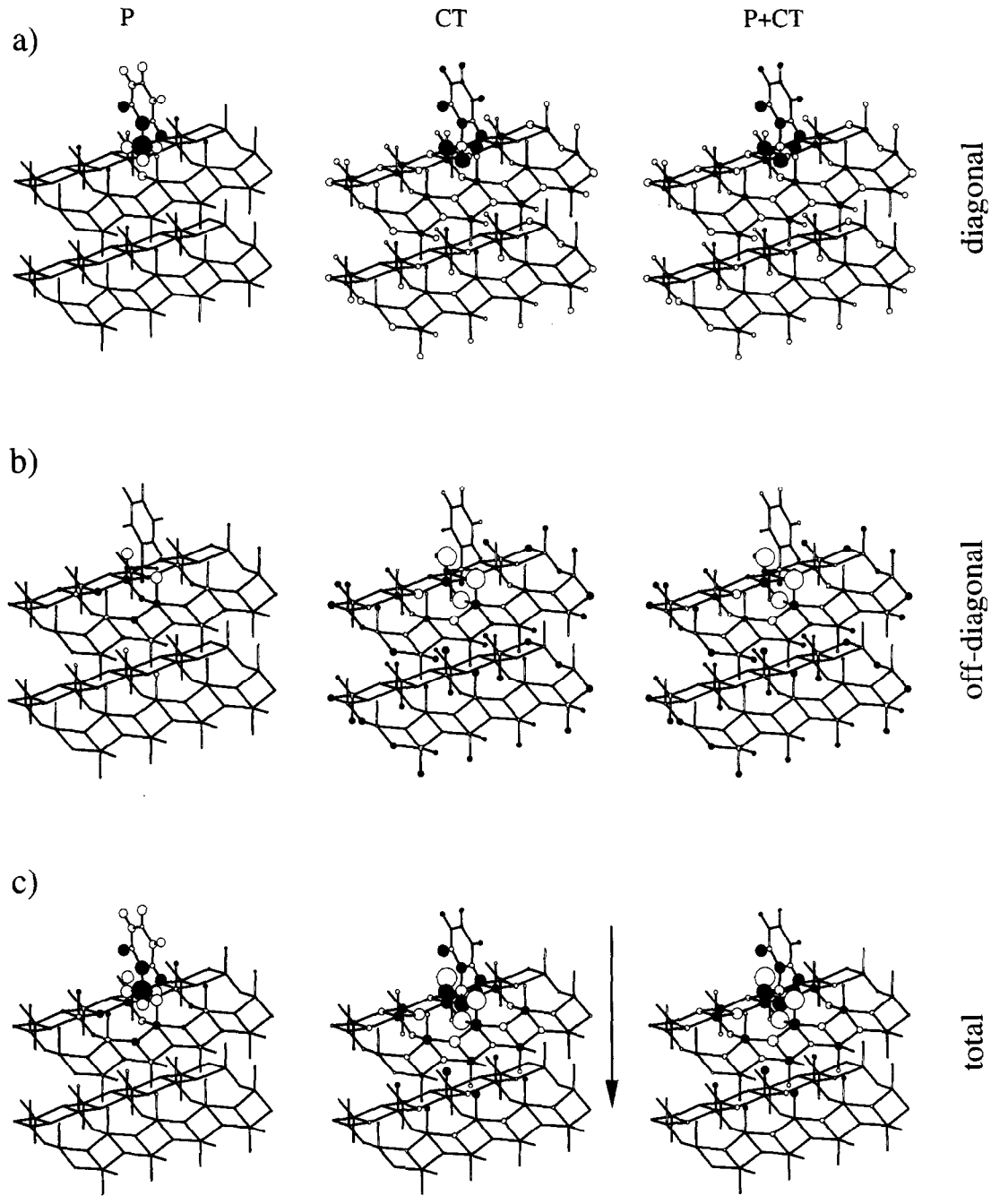

Fig. 3. The representative resolution of the isoelectronic total (third row) polarizational (P, first column), charge transfer (CT, second column), and overall (P + CT, third column), electron population diagrams, into the diagonal (first row) and off-diagonal (second row) contributions, for the perpendicular adsorption of toluene on the $O_{(2)}$ oxygen on the top layer (see Fig. 1b and Fig. 2c). For reasons of clarity both layers have been shifted one relative to the other by an arbitrary mutual translation. The same scale factor has been used in all three panels of each column. Throughout the paper the open and black circles correspond to the positive and negative values, respectively, and the circle area reflects the magnitude of the populational shift; the arrows in the total CT diagrams show the CSA direction of the inter-reactant CT.

layers of the cluster in Figs. 3–8 by an arbitrary relative translation. These results are based upon the charges obtained from the semi-empirical SINDO1 [19] calculations. The geometric structure of the large cluster involves the SINDO1 optimized intra-layer bond lengths [14] and the crystallographic values of the bond angles and the inter-layer V–O bond length.

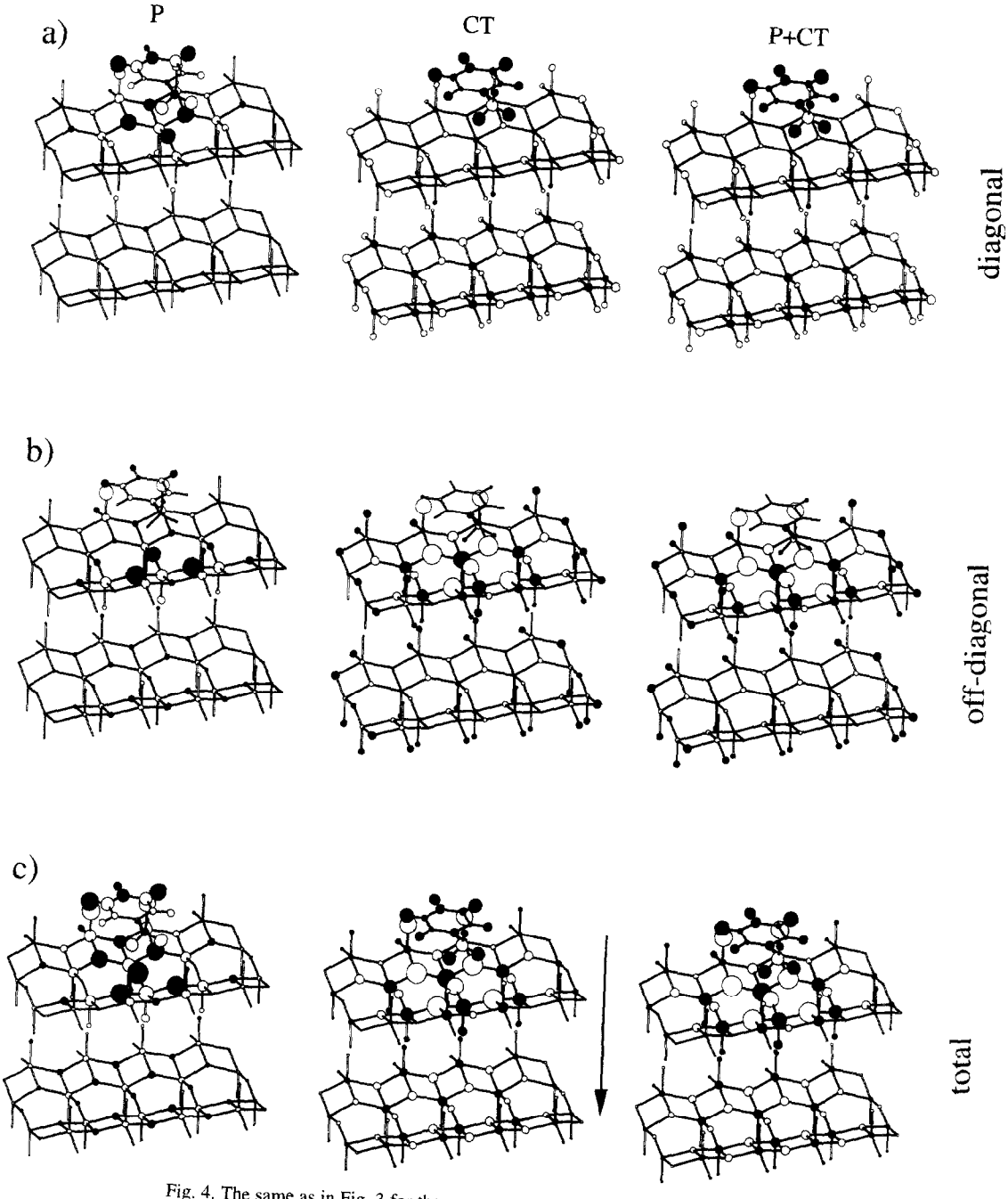

Fig. 4. The same as in Fig. 3 for the representative parallel coordination of Fig. 2f.

Atomic units are used unless specified otherwise.

4. General discussion

4.1. Energetical considerations

It follows from the previously reported semi-empirical SCF MO (scaled-INDO [20]) energies, for the selected toluene–$[V_2O_5]$ systems involving very small non-stoichiometric surface clusters [13], that the parallel adsorption above the vanadium site (Fig. 2f) generates much stronger chemisorption bond than the remaining perpendicular adsorptions considered in this analysis (Fig. 2(a–c, e)), which generate comparable interaction energies. These values, determined for the optimum inter-reactant separation, when no geometry relaxation is allowed, are ordered in the qualitative sequence:

$$E(2f) \ll E(2c) < E(2e) < E(2b) < E(2a);$$

scaled-INDO. (10)

This overall energetical hierarchy can be supplemented by the qualitative CSA predictions from Eq. (9). These crude estimates predict at the shorter interreactant separation internal charge instability ($E_{CT} > 0$) for all structures in Figs. 5 and 6, but that in Fig. 2a. At the larger separations (Fig. 5d and Fig. 6(b, d, f)) all systems are diagnosed as internally stable ($\eta_{CT} > 0$, $E_{CT} < 0$); the corresponding total energies (ES + P + CT) identify the arrangement of Fig. 2f as the most stable one, with the remaining two parallel complexes giving lower magnitudes of (comparable) stabilization energies.

The E_{ES} contributions in the structures of Fig. 5(d–f) and Fig. 6(a, e, f) are positive; they are stabilizing in all remaining cases; relatively large polarization contributions are detected in the arrangements of Fig. 5c and f. The qualitative CSA energetical hierarchies for perpendicular complexes in Fig. 5 are:

$$\begin{aligned} E_{ES}(c) < E_{ES}(b) < E_{ES}(a) < E_{ES}(a') \sim E_{ES}(b') \\ < E_{ES}(e) \sim E_{ES}(e') \sim E_{ES}(f') \sim E_{ES}(d) \\ < E_{ES}(f); \end{aligned} \quad (11)$$

$$\begin{aligned} E_{ES+P}(c) \ll E_{ES+P}(f) \ll E_{ES+P}(e) \\ \ll E_{ES+P}(b) < E_{ES+P}(a) < E_{ES+P}(d) \\ < E_{ES+P}(a') < E_{ES+P}(e') < E_{ES+P}(f') \\ < E_{ES+P}(b'); \end{aligned} \quad (12)$$

$$\begin{aligned} E(c) \ll E(d) \ll E(a) \ll E(e') < E(f') < E(e) \\ \sim E(b') \ll E(a') < E(f) < E(b), \end{aligned} \quad (13)$$

where the prime denotes the larger internuclear distance case (not shown in the figure). The corresponding sequences for Fig. 6 read:

$$\begin{aligned} E_{ES}(c) < E_{ES}(b) \sim E_{ES}(d) < E_{ES}(f) < E_{ES}(e) \\ < E_{ES}(a); \end{aligned} \quad (14)$$

$$\begin{aligned} E_{ES+P}(a) < E_{ES+P}(e) < E_{ES+P}(c) \sim E_{ES+P}(b) \\ < E_{ES+P}(d) < E_{ES+P}(f); \end{aligned} \quad (15)$$

$$E(b) \ll E(d) \sim E(f) \ll E(a) \ll E(e) \ll E(c). \quad (16)$$

Of interest in the theory of chemical reactivity also is a qualitative comparison of the energetical preferences at a comparable separation between reactants. At the earlier stage of the adsorbate approach one obtains the following sequences of total CSA interaction energies (given in parentheses) (see Eqs. (13) and (16)):

(i): for perpendicular structures of Fig. 5:

$$\begin{aligned} d(-1.145) \ll e'(-0.386) < f'(-0.337) \\ < b'(-0.237) < a'(-0.196); \end{aligned} \quad (13a)$$

(ii): for parallel structures of Fig. 6:

$$b(-1.235) \ll d(-0.461) \sim f(-0.456). \quad (16a)$$

At the close approach structures the corresponding orderings are:

$$\text{(i)}: c(-2.572) \ll a(-0.754) \ll e(-0.249) < f(-0.075) < b(-0.198); \quad (13b)$$

$$\text{(ii)}: a(-0.198) \ll e(0.325) \ll c(1.166). \quad (16b)$$

Thus, the structures 5c (2c) and 6b (2f) are predicted to constitute the CSA energetically most favorable perpendicular and parallel adsorption arrangements, respectively. This qualitatively agrees with the scaled-INDO calculations on much smaller clusters, which we have summarized at the beginning of this section. Notice, that at an earlier approach, the parallel structure of Fig. 6b exhibits lower interaction energy than the most stable perpendicular arrangement of Fig. 5d.

4.2. Relative role of the diagonal and off-diagonal isoelectronic responses

A reference to Fig. 3 shows that the total charge response patterns for the perpendicular adsorption of toluene on the bridging $O_{(2)}$ site of the top layer (Fig. 2c) have a common structure at all stages of the charge reconstruction. Namely, the total patterns (third row) in the figure are seen to be dominated by the respective diagonal contributions of the adsorbate (first row) and the off-diagonal contributions of the substrate (second row). The same general rule has been observed in the remaining perpendicular coordinations. At the larger separation between reactants the internal CT is from the toluene (B) to cluster (A), due to rather weak overall charge coupling between reactants. In the overall description level (third column) the resultant effect of the P and CT displacements is shown; these contributions may enhance each other, e.g., in the ring fragment in the vicinity of the methyl group or in the two $V-O_{(1)}$ fragments of the surface in the chemisorption region, or they may reduce one another, e.g., on the methyl hydrogens and the remaining, peripheral part of the benzene ring. The total P and CT shifts are seen to act mainly 'in phase', with the exception of the methyl group, where the dominating CT pattern is partly reduced by the P-component. A comparison between the respective panels in the three columns of the figure reveals that the toluene → cluster CT-induced charge displacements dominate the overall (P + CT) trends.

There is a strong localization of the in situ responses, which exhibit the largest magnitudes of the AIM charge displacements in the chemisorption region, with only marginal participation of the supporting layer and peripheral atoms of the surface layer. As also seen in the figure, only the $O_{(1)}$ sites of the second layer are more strongly involved in moderating the primary charge shifts in the chemisorption region of the surface layer.

Similar conclusions follow from Fig. 4. For this parallel arrangement (Fig. 2f, larger distance between reactants) the second layer plays a quite substantial role in the cluster reconstruction, particularly at the CT stage. Again, the total patterns of the third row are roughly the combinations of the diagonal charge shifts in toluene and the off-diagonal charge displacements in the surface layer of the cluster, at all stages of description. A general similarity of the respective panels in the CT and (P + CT) columns indicates that the toluene → cluster CT component is the dominant one in this particular chemisorption arrangement.

4.3. Direction of the inter-reactant charge transfer

It follows from Eq. (6) that the interaction between reactants at finite separations may change the sign of $\mathcal{N}$, relative to the corresponding separated reactants estimate, since both the chemical potential difference ('force') and the CT hardness ('stiffness modulus') in Eq. (6) are interaction dependent. There is always a strong relaxational influence of the cluster upon

the toluene chemical potential, while the opposite influence is relatively weak. For example in the perpendicular structure of Fig. 2f (6b) the CSA predicted levels of the polarized reactant chemical potentials are: $\mu^{(+)}_{\text{toluene}} = -0.0807$ and $\mu^{(+)}_{\text{cluster}} = -0.2532$; these values can be com-

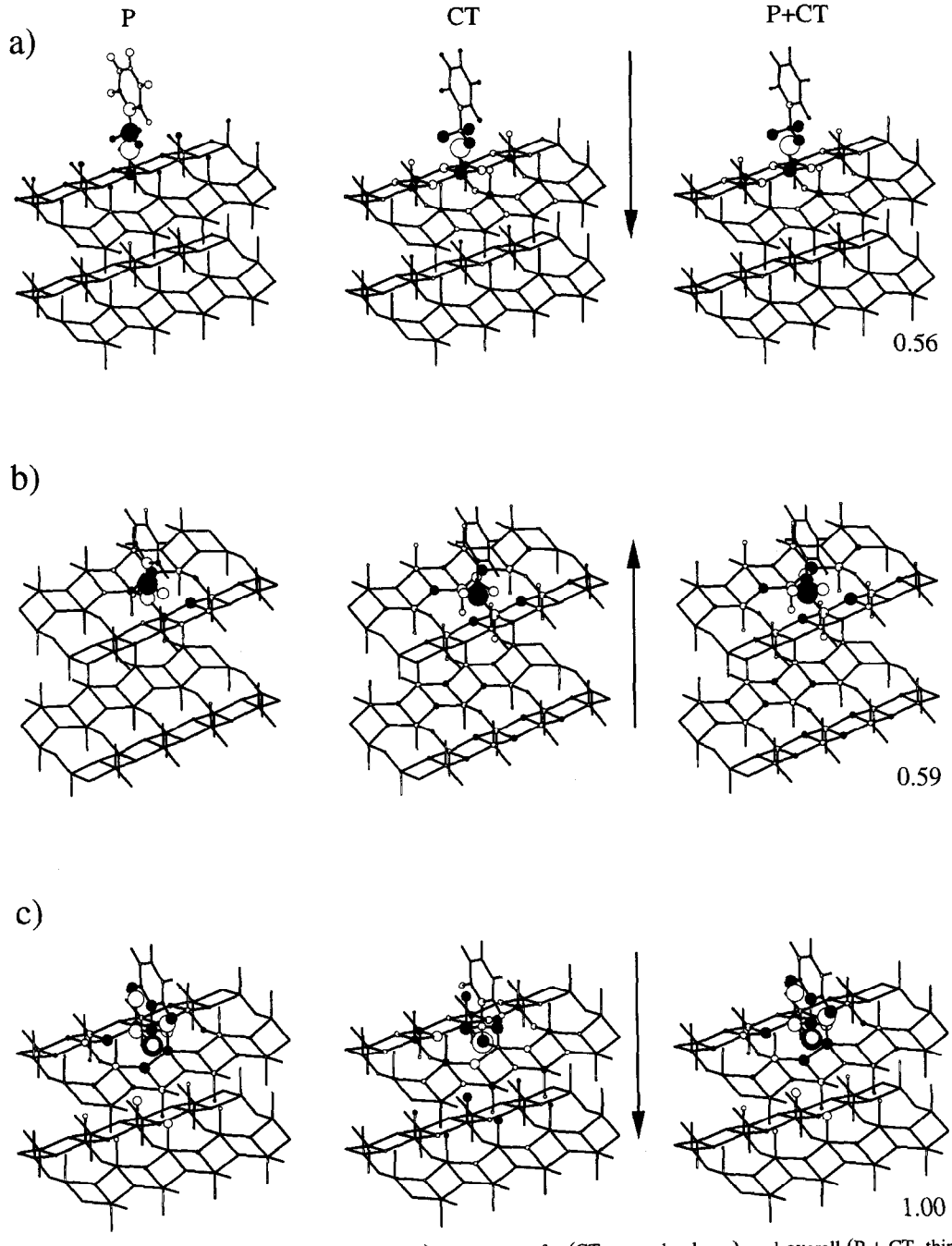

Fig. 5. The total (isoelectronic) polarizational (P, first column), charge transfer (CT, second column), and overall (P + CT, third column), electron population diagrams for perpendicular coordinations of Fig. 2. Rows (c, d) display plots for two representative distances of toluene from the $O_{(2)}$ adsorption site in the chemisorption arrangement of Fig. 2c. The numbers below the overall diagrams indicate the scale factor to be used to multiply the overall diagrams in the figure to bring them to the common scale of the row c.

pared with the separate reactant estimates from the same canonical $\{\mathbf{u}_X^0$ and $\eta^{X,X}\}$ input data: $\mu^0_{\text{toluene}} = -0.2542$ and $\mu^0_{\text{cluster}} = -0.2524$ (the chemical toluene cluster potential discontinuity [3,21] has not been included).

A reference to Figs. 3–6 shows that indeed

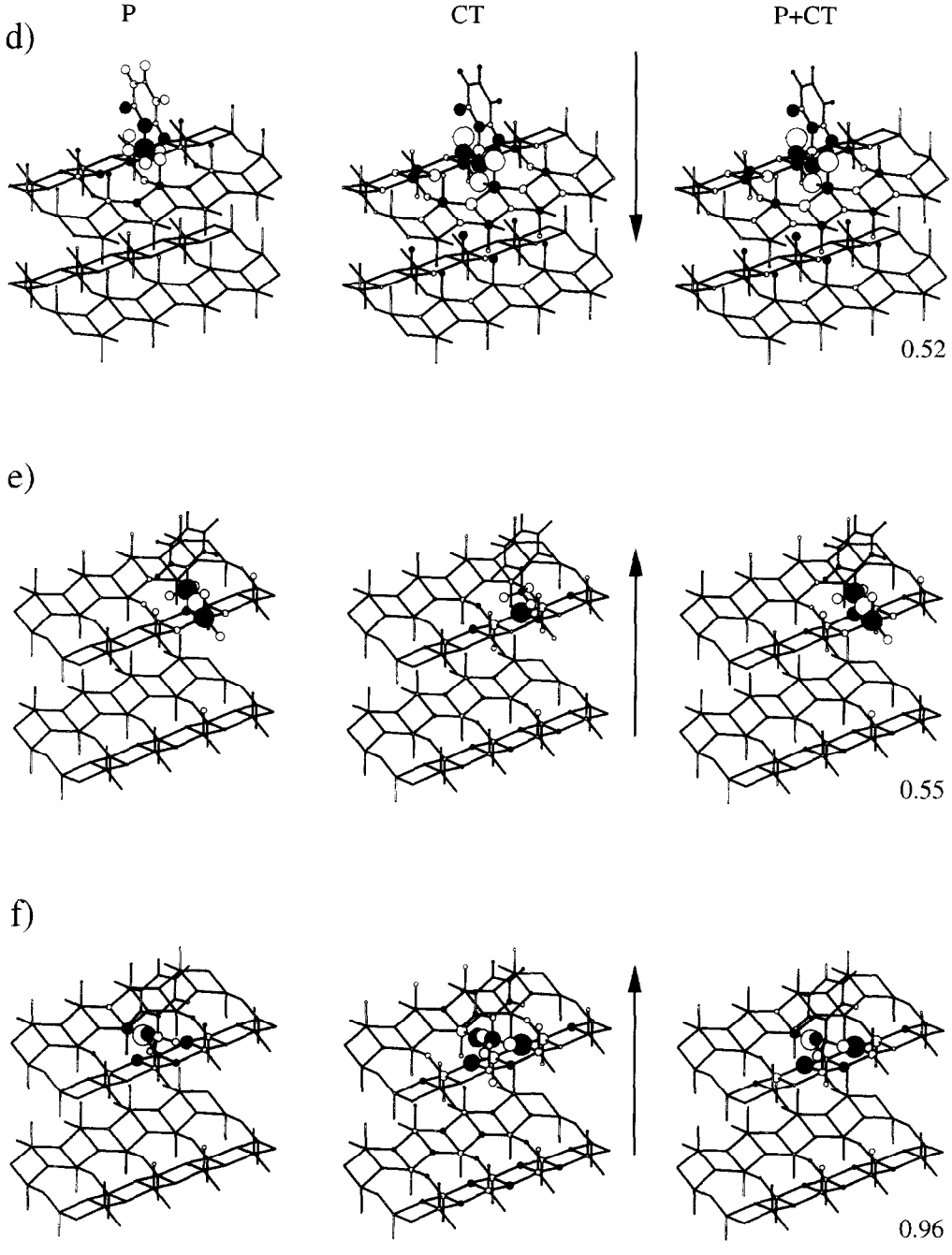

Fig. 5 (continued).

both directions of the CT are predicted. For example, in the parallel arrangements of toluene (Fig. 6), the strongly interacting complexes (at the shorter distance between reactants, panels a, c, e) exhibit the cluster (B) → toluene (A) CT, reversed in comparison with that found in the weakly interacting complexes (at the larger separation, panels b, d, and f).

In the perpendicular structures (Fig. 2(a–e)) at the larger inter reactant separations a com-

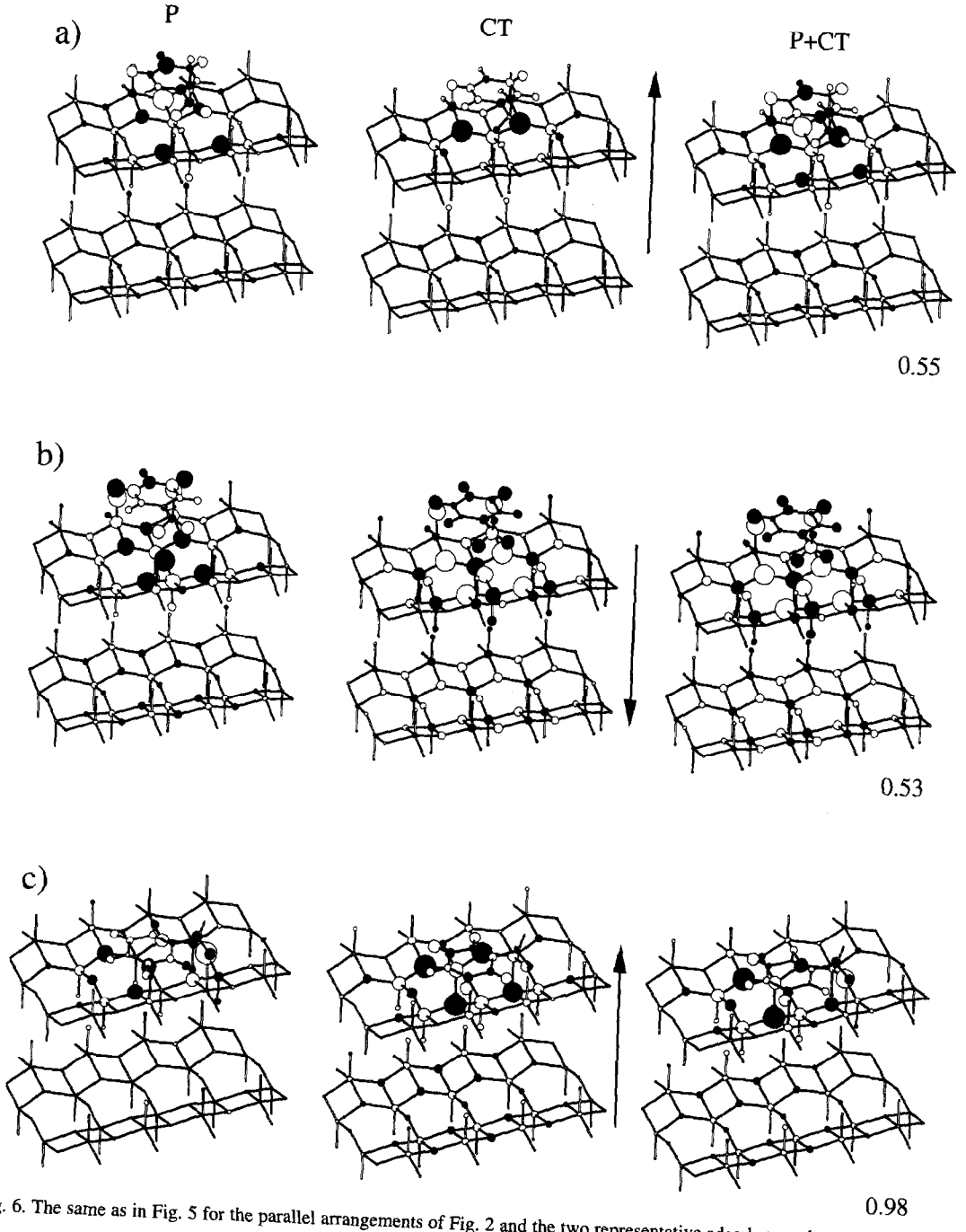

Fig. 6. The same as in Fig. 5 for the parallel arrangements of Fig. 2 and the two representative adsorbate–substrate distances.

mon toluene → cluster CT direction is predicted from the CSA calculations. For the close approach complexes of Fig. 5(a–c, e, f), for which the interreactant perturbation becomes stronger, this direction is reversed in panels b, e, and f.

4.4. Relative role of the P- and CT-components in the overall isoelectronic responses

A reference to Fig. 5 shows that in most cases the CSA predicted responses are indeed

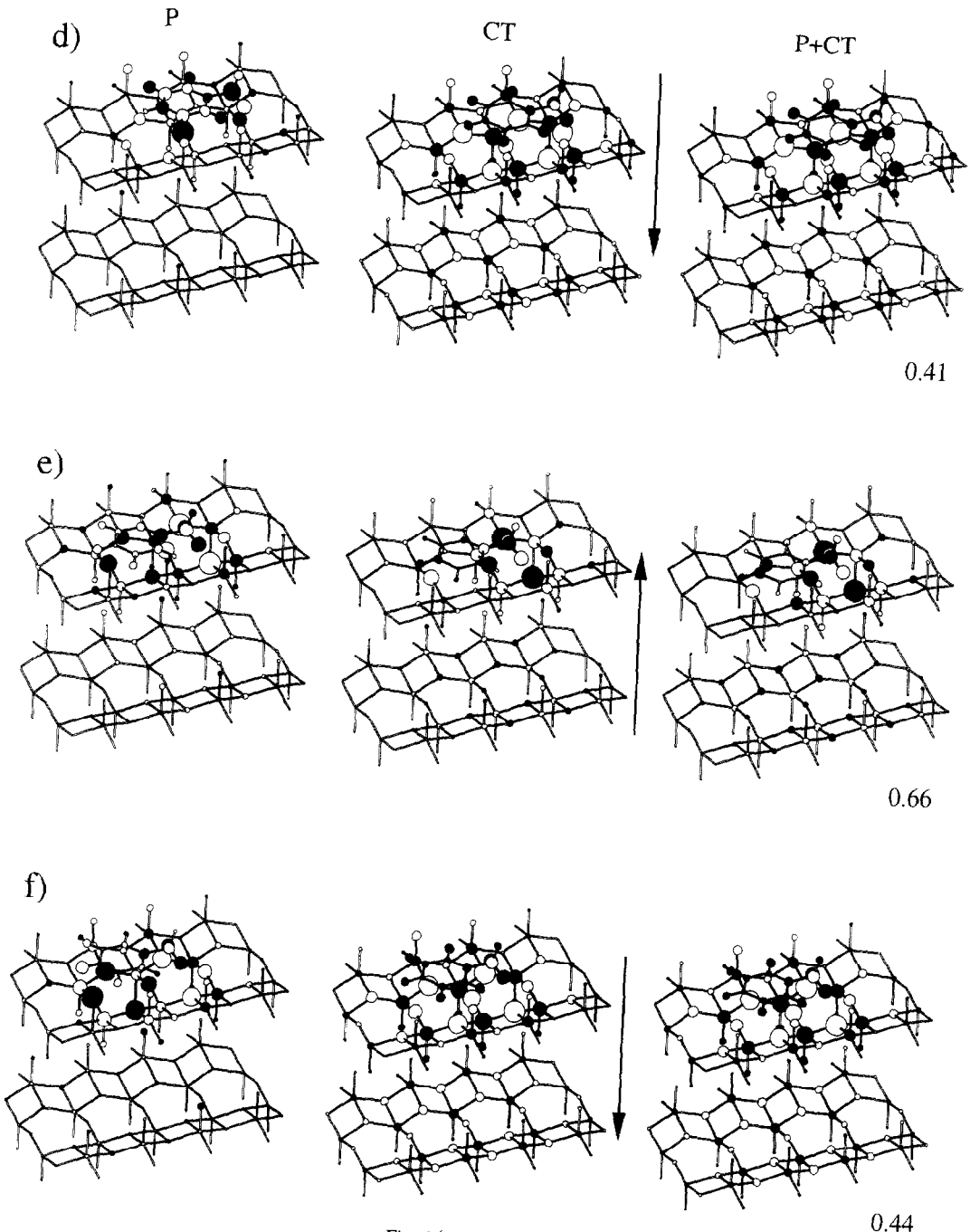

Fig. 6 (continued).

dominated by the CT-component. However, there are important exceptions to this rule at some close approach structures. For example, an inspection of the three panels of Fig. 5c shows that it is the direct polarization, before the CT, which determines the gross features of the overall charge reconstruction pattern. It should be observed, that at the larger internuclear separation for the same chemisorption arrangement (Fig. 5d) the CT-component alone generates qualitatively correct charge reconstruction diagram. Additional examples of a dominant role of the reactant mutual polarization can be found in Fig. 5e and f.

Similar cases can be found in Fig. 6, although in most cases, particularly at larger separations, it is the CT component that determines the most important features. An example of a strong P contribution to the overall pattern is found in Fig. 6a, where both components enhance each other on atoms undergoing the largest charge displacements. When the distance increases (Fig. 6b) both components act with opposite phases on most of the cluster sites in the chemisorption region. Similarly, in Fig. 5f the opposite displacements on the corresponding $O_{(3)}$ surface sites in the P diagram, have only a minor effect of differentiating the four such sites in the chemisorption area; this is a clear sign of a strong CT dominance of the overall charge reconstruction pattern due to the chemisorption.

5. Mutual polarization of reactants

In this section we shall examine the charge polarization patterns of the left (P) columns in Figs. 5 and 6; the bond weakening/strengthening implications of these polarizational changes will also be summarized.

The P diagram of Fig. 5a predicts a flow of electrons from the methyl group to the benzene ring in the toluene and the accompanying (bond weakening) $V \rightarrow O_{(1)}$ polarization of the vanadyl adsorption site. These trends are further enhanced at the CT stage, as shown in the middle diagram of Fig. 5a, via the polarization induced by the predicted toluene → cluster CT. The ring carbons are only weakly affected in the P-diagram during the adsorption on the $O_{(1)}$ site, with the exception of the substituted ring carbon, which acquires relatively more electrons; this should strengthen the hyperconjugation π-component between this atom and the methyl group.

It follows from Fig. 5b that the direct polarization diminishes the electron population of the methyl carbon; the electrons are shifted mainly to its nearest neighbors. The $O_{(2)}$ adsorption site increases its negative charge at the expense of the nearby V and $O_{(3)}$ sites; this should weaken the $V-O_{(2)}-V$ bonds, since it reverses the original net $O_{(2)} \rightarrow V$ donation of these coordination bonds. Again, the polarizational influence upon the ring is predicted to be rather small. It should be observed that the next (CT) diagram predicts a reversal of the main P trends in the surface chemisorption region, as a result of the subsequent cluster → toluene CT.

A reference to the P diagram of Fig. 5c shows that in this case the polarizational influence is more extended. Namely, in addition to the $V \rightarrow O_{(1)}$ bond polarization (weakening), due to the presence of the *ortho*-hydrogens of the ring, the $O_{(2)}$ adsorption site is hardened by the presence of the softer methyl hydrogens which acquire electrons from the methyl carbon and the benzene ring. Such a polarization promotes the subsequent $(C)H_3 \rightarrow O_{(2)}$ and $O_{(1)} \rightarrow H_{ortho}$ flows accompanying the toluene → cluster CT (see the next diagram).

In Fig. 5d one detects an extra accumulation of electrons on the methyl hydrogens and in the peripheral part of the toluene, at the expense of the $(H_3)C-C$ carbons and the *ortho*-hydrogens. This polarization of toluene weakens the C–H bonds in the coordinating methyl group, since it partly reverses the $H \rightarrow C$ polarization in the isolated adsorbate. One also observes in the same diagram that the $O_{(1)}$ and $O_{(2)}$ active sites on the surface acquire electrons from the coor-

dinating metal sites (weakening of the $V-O_{(1)}$ bonds). This mutual polarization creates favorable conditions for the subsequent transfer od electrons from the methyl hydrogens to these oxygen sites, detected in the CT diagram of Fig. 5d.

A comparison of the P diagrams of structures c and d of Fig. 5 shows that the pattern of polarizational changes is qualitatively similar, with the exception of the $O_{(2)}$ site, which exhibits different displacements for the two interreactant separations.

The next P diagram of Fig. 5e refers to the toluene coordination on $O_{(3)}$. Here the toluene polarization is practically limited to the methyl group; it is seen to shift electrons from the methyl carbon towards hydrogens facing the vanadium sites. The surface undergoes a complementary $V \rightarrow O$ charge reconstruction in the most perturbed VO_5 pyramid. The corresponding CT diagram reveals that these changes are further enhanced at the cluster → toluene CT stage.

Finally, the CSA calculations for the toluene adsorption on vanadium site (Fig. 5f) also predict strongly localized polarizational responses at the physisorption stage. The range of these changes covers the methyl group (shifting electrons away from the hydrogen facing the nearby $O_{(2)}$ site), and the two surface pyramids linked through the $O_{(2)}$ bridge (shifting electrons to the bridging oxygen, i.e., weakening the $V-O_{(2)}$ bonds). One therefore observes a degree of differentiation of both the methyl hydrogens and lattice oxygens, which should create favorable conditions for the $O_{(2)} \rightarrow$ methyl $\leftarrow O_{(3)}$ coordination at the CT-stage of the chemisorption process.

Let us examine now the P diagrams of Fig. 6. In the first structure of part a the electrons are accumulated at the *meta*-hydrogens, *ortho*-carbons and the two methyl hydrogens facing a pair of the $O_{(3)}$ sites. The active sites of the surface undergo complementary polarizational shifts: the $O_{(3)}$ sites below the toluene hydrogens lose electrons, which are shifted towards the vanadium atom below the ring center (strengthening of these $V-O_{(2)}$ bonds) and the $O_{(3)}$ atom below the C–H *para*-fragment accumulates electrons at the expense of the nearby vanadium sites (weakening of these V–O bonds); these charge reconstruction displacements, creating favorable conditions for a selective oxidation in the *para*-position and on the methyl group, are seen to be enhanced at the CT stage (see the next diagram in Fig. 6a).

This direct polarizational pattern changes with the increase in the toluene–surface separation (Fig. 6b). The main displacements in the physisorbed toluene now involve the increase of the electron charge on the *meta*-carbons and the two methyl hydrogens directed towards the $O_{(3)}$ surface sites. In the cluster the two VO_5 pyramids located below toluene exhibit a strong enhancement of the original $O \rightarrow V$ coordination bonds (bond strengthening) and the two vanadyl fragments in the vicinity of the *meta*-hydrogens of the ring accumulate electrons. These terminal $O_{(1)}$ oxygens will further receive electrons at the CT stage, while most of the other surface polarization trends will be reversed in the toluene → cluster CT.

In the close-approach parallel complex of Fig. 6c the ring atoms mainly gain electrons from the methyl group, but the changes are relatively minor in comparison with the surface charge shifts. The latter exhibit a strong accumulation of electrons on the bridging oxygen below the methyl group, which should facilitate a selective oxidation of the methyl group by this lattice oxygen, and a decrease of the electron population of the $O_{(2,3)}$ sites below the opposite toluene fragment. We would like to emphasize the reverse shifts exhibited by the $O_{(3)}$ surface sites facing the *ortho*- and *meta*-hydrogens of the toluene ring.

When the distance between reactants is increased (see Fig. 6d) a relatively strong ring and methyl group polarizations are predicted. In the ring they strengthen the C–H and $C_{ortho}-C_{meta}$ bonds, while weakening the remaining bonds. Similarly, in the methyl fragment the C–H bonds

are weakened as a result of a partial reversal of the original (isolated toluene) bond polarization. The complementary polarization of the cluster surface layer is more delocalized; the main displacements represent a shift of electrons from the bridging $O_{(2)}$ sites to the nearby oxygen and vanadium atoms. At this P stage, therefore, no substantial release of the above bridging oxygens is predicted, since they become more strongly bonded to the coordinating vanadium atoms as a result the reactant mutual polarization.

Finally, let us examine the P plots for the parallel complexes of Fig. 6(e, f). A comparison of these two diagram reveals that in this case the P pattern remains qualitatively unchanged, when the inter-reactant separation increases. The main polarization trends of toluene involve the two C–H bond strengthening in the methyl fragment, and an overall accumulation of electron in the ring, with the exception of the substituted carbon. The surface exhibits larger polarizational flows, which shift electrons mainly to the $O_{(2,3)}$ sites below the methyl side of the toluene from the $O_{(2,3)}$ locations below the other end of the adsorbate. The electron gaining surface oxygens become weakly bonded by the coordinating vanadium sites (a partial reversal of the original coordination), and thus are more accessible for the toluene oxidation.

6. Internal charge transfer induced displacements

In this section we examine in some detail the internal CT-induced charge reconstructions shown in the middle columns of Figs. 5 and 6.

Consider first the perpendicular adsorption on the vanadyl oxygen of the top layer surface (Fig. 2a and Fig. 5a). The phases of populational displacements in the region of the surface bond are similar to those observed at the P stage, with the methyl group hydrogens losing electrons and the $O_{(1)}$ atom gaining electrons, as expected in the $-CH_3 \rightarrow O_{(1)}$ coordination. No appreciable participation of the ring and the second layer atoms is predicted for this internal CT process. The predicted surface reconstruction displacements involve a substantial $V \rightarrow O_{(1)}$ polarization (further weakening of this bond) and a slight increase in the electron population of remaining oxygen sites in the chemisorption region. The effective range of appreciable charge reorganization created on both reactants by this CT practically does not extend much beyond the methyl group and the coordinating VO_5 pyramid.

The opposite CT charge reorganization is observed in the middle panel of Fig. 5b, corresponding to the perpendicular adsorption on the bridging oxygen of the bottom layer surface (Fig. 2b). This is due to the reverse, cluster → toluene internal CT. The $O_{(2)}$ adsorption site also affects mainly the methyl group in the toluene; again, the cluster is seen to respond only on the surface, in the vicinity of the adsorption site. Both the $O_{(2)}$ adsorption site and the nearby $O_{(3)}$ atoms net donate electrons to the methyl hydrogens and the vanadium atoms, thus becoming more strongly bonded. It should be observed, that this charge displacement on $O_{(2)}$ partly reverses that observed at the P stage in the same complex. The overall polarizational matching of the AIM population shifts in the chemisorption region of the CT panel of Fig. 5b, with the donor atoms of the basic reactant (cluster) facing the acceptor atoms of the acidic reactant (toluene), indicates a relatively soft charge reconstruction.

Next two CT diagrams of Fig. 5(c, d) correspond to the perpendicular adsorption on the bridging oxygen of the top layer surface (Fig. 2c). A reference to the CT panels of Fig. 5(c, d) shows, that the pattern of main charge readjustments in the methyl group, and in the $[VO_5]$–$O_{(2)}$–$[VO_5]$ adsorption region of the surface, only slightly changes with the distance between reactants. It should be noted that in both cases the same toluene → cluster CT-direction is predicted. At both distances the same $-(C)H_3 \rightarrow O_{(2)}$ charge shift ('forward chemisorption dona-

tion') is detected. At the close approach arrangement of Fig. 5c one also finds the $(VO_{(1)}) \rightarrow H_{ortho}$ 'chemisorption back donation', which is reversed at the larger distance between reactants in Fig. 5d. The other observed difference is the C(ring) → $C(H_3)$ bond polarization in Fig. 5d, which weakens this C–C bond by reducing its original polarization in the isolated toluene and partially reversing the hyperconjugation donation from methyl to the π bond system of the ring. In Fig. 5c both these carbon atoms are predicted to gain electrons during the toluene → cluster CT, so that this C–C bond is not predicted to be appreciably affected by the toluene → cluster coordination.

It should be observed that at the larger separation, reactants the methyl group hydrogens are placed closer to the vanadyl oxygens of the surface, so that in Fig. 5d they effectively coordinate to both $O_{(1)}$ and $O_{(2)}$ sites. A formation of partial $O_{(1)} \leftarrow H_{ortho}$ bonds implies an effective removal of electrons from the $(C–H)_{ortho}$ bond region, which weakens the covalent bond component and strengthens the ionic bond order. This also suggests a relatively facile activation mechanism of a possible breaking of the methyl C–H bonds and forming the O–H bonds in this chemisorption arrangement. In Fig. 5(c, d) the layer-bridging oxygens are seen to be involved more strongly than in previous perpendicular complexes, even at the larger separation between reactants.

The perpendicular adsorption on the triply coordinated oxygen of the bottom layer surface (Fig. 2e) generates the CT-diagrams of Fig. 5e, in which the surface donates electrons to the toluene. It should be observed that, similarly to the 5b CT pattern, the oxygen adsorption site donates electrons to the nearby vanadium sites (bond strengthening) and to the methyl hydrogens. This polarization is qualitatively similar to that seen at the P stage (left diagram). The $O_{(3)}$ adsorption site is therefore more tightly bonded on the surface; thus, its subsequent participation in the toluene oxidation is less probable. Also, a formation of the surface bond with the methyl hydrogens is seen to have only a minor effect upon the C–H bonds in this CT process. The net increase in the electron populations of the 'bridging' hydrogens in this perpendicular complex prevents a weakening of the C–H bonds, while providing at the same time an extra 'coordination' bond component $O_{(3)} \rightarrow H$ responsible for the chemisorption bond.

When toluene is perpendicularly adsorbed on the vanadium atom (Fig. 2f and Fig. 5f), the methyl hydrogens acquire electrons from the $O_{(2)}$ and $O_{(3)}$ surface sites and the methyl carbon; these CT-induced charge shifts stimulate a dissociation of the C–H bonds of the methyl group, and a formation of the surface O–H group.

Finally, let us examine the CT-diagrams of Fig. 6, corresponding to the parallel adsorption arrangements on the bottom layer surface (Fig. 2(f–h)). The two probing inter-reactant distances, representing the close and earlier (more distant, by 1 Å) stages of the parallel approach of the toluene ring to the VO_5 pyramid bases, are considered in parts (a, c, e) and (b, d, f), respectively.

Consider first the chemisorption structures of Fig. 2f (Fig. 6(a, b)). A comparison between the CT panels of Fig. 6(a, b) indicates, that even at the larger distance both toluene and cluster are strongly affected. These two diagrams are qualitatively different, though, due to the reverse inter-reactant CT they correspond to. At the closer approach (Fig. 6a) electrons are removed mainly from the two $O_{(3)}$ sites below the *ortho*- and *meta*-hydrogens of the ring, and shifted to *ortho*- and *meta*-CH fragments of toluene and to the vanadium surface sites. This pattern therefore implies a strengthening of the V–O bonds in the adsorption region of the surface. The net inflow of electrons to the ring must populate the antibonding π^* orbitals, thus facilitating the ring destruction. This chemisorption exerts practically no influence upon the methyl fragment of toluene.

At the larger distance (Fig. 6b) all ring bonds are also predicted to be weakened by an effec-

tive removal of electrons from all atoms, including the bonding electrons of the π C–C bonds. This can also promote the total degradation of the ring structure, and ultimately the nonselective, total oxidation of the toluene [13]. The major toluene reconstruction trends now also include a substantial H → C bond strengthening polarization of the methyl substituent; hence the methyl part of the adsorbate is not predicted to be activated at the CT stage in this parallel complex. On the surface one detects a strong charge reconstruction in the adsorption region, involving various degrees of the V → O back donation, which weakens the O → V coordination bonds. Therefore, these $O_{(2,3)}$ lattice oxygens become accessible for oxidizing the toluene. The increase of the positive charge of the toluene hydrogen atoms and the accompanying increase in the negative charge of the surface oxygen sites should effectively strengthen the overall electrostatic (ionic) component of the resultant toluene–cluster bond. This is indeed reflected by the total energy of this structure in Eq. (16). The second layer reaction to the chemisorption in the CT panel of Fig. 6b is similar to that observed in the surface layer, but much weaker.

In the second mutual arrangement of the 'parallel' oriented reactants (Fig. 2g and Fig. 6(c, d)) the CT diagrams predict a strengthening of the V–O bonds in the chemisorption region in the close-approach case (Fig. 6c) and their weakening for the larger inter-reactant separation (Fig. 6d). The toluene ring patterns also exhibit a general change in the phases of atomic displacements, when this distance increases. Obviously, this is caused by the reverse directions of the inter-reactant CT in both these complexes. An inspection of these two CT diagrams also shows that the C_{ortho}–C_{meta} and $(C–H)_{ortho,meta}$ bonds in the ring are weakened in Fig. 6c, due to a removal of electrons and the reversal of the initial bond polarization, respectively. In Fig. 6d the electrons are withdrawn from the ring, similarly to the CT pattern in Fig. 6b; this also implies a general bond weakening. Moreover, as in the previous parallel arrangement, the methyl substituent practically does not participate in the interreactant CT in the short-separation complex, while its polarization at the earlier approach stage strengthens the C–H bonds. The above activation trends again suggest a tendency towards the ring degradation and a possible involvement of the lattice oxygens in the toluene oxidation in the structure of Fig. 6d.

Let us finally examine the two CT diagrams of Fig. 6(e, f) corresponding to the third parallel arrangement of Fig. 2h. The main features of the CT pattern in Fig. 6e are the methyl bond weakening reconstruction in toluene, and the surface V–O bond strengthening in the surface layer of the cluster, in the vicinity of the methyl group; both these trends should facilitate a selective oxidation of the methyl part of toluene by the lattice $O_{(2,3)}$ oxygens. With the increase in the substrate–adsorbate separation (Fig. 6f) the CT pattern changes: the range of the surface reconstruction increases, with the dominant V → O bond weakening polarization, the electrons are removed from the ring (general bond weakening) and the CH methyl bonds are strengthened. Therefore, only at the close-approach structure the selective oxidation of toluene should be expected in this parallel arrangement.

7. Toluene activation and surface reconstruction trends from overall diagrams

In this section we briefly comment on the implications of the (P + CT) diagrams of Figs. 5 and 6, by identifying the dominant component of these overall plots. The CT component dominates the overall charge reorganization patterns in Fig. 5(b, d) and Fig. 6(b, c, d, e, f) while the P component dominates in the overall diagrams of Fig. 5(c, e, f); in the remaining structures of Fig. 5a and Fig. 6a both components are comparable and generally display the same phases of the main AIM displacements. With an increase

in separation between reactants the polarization component decays faster than the CT one. Therefore, one generally observes the CT domination at the earlier stage of the adsorbate approach to the surface, while the P component contributes more strongly at shorter distances. Clearly, the toluene activation/surface reconstruction implications of the dominant component, described in detail in the preceding two sections, remain valid for the overall charge reconstruction.

Consider first the perpendicular adsorption systems. The weakly bonded $O_{(1)}$ lattice oxygen in Fig. 5a is expected to form a bond with either the methyl hydrogen or carbon, since the C–H bond dissociation is promoted in this adsorption arrangement. In Fig. 5b, where $V–O_{(2)}–V$ bonds are strengthened and the C–H methyl bonds are weakened, the dissociation in the coordinating methyl group can be expected. The forward ($H_{ortho} \rightarrow O_{(1)}$) and back ($O_{(2)} \rightarrow H_3$) donations are clearly seen in Fig. 5c. This promotes the dissociation of the C–H bonds in the methyl and *ortho*-ring positions. The $O_{(1)}$ lattice oxygen participation in the selective oxidation is also highly probable, due to their being less strongly bonded to the vanadium atoms in the chemisorption system. These trends partially change in Fig. 5d, where the two forward donation channels, $H_{ortho} \rightarrow O_{(1)}$ and $H_{(3)} \rightarrow O_{(2)}$, are detected. Therefore, in this particular case both these lattice oxygen sites become accessible for the toluene oxidation; also, since the methyl hydrogens are seen to donate their electrons mainly to the surface oxygen sites the C–H bond breaking at both the *ortho*-position in the ring and in the methyl group may be expected in this energetically favorable chemisorption complex. In Fig. 5e only the methyl substituent is activated (bond weakening). Finally, in Fig. 5f the two methyl hydrogens are involved in the $O_{(3)} \rightarrow H$ back donation, while the third hydrogen donates electrons to the surface bridging oxygen: $H \rightarrow O_{(2)}$. Both these channels may lead to the C–H bond dissociation; however, only the $O_{(2)}$ site is chemically more accessible for oxidizing the toluene, since the $O_{(3)}$ atoms are predicted to be more strongly bonded to the coordinating vanadium sites.

Let us similarly summarize the main reactivity trends implied by the (P + CT) column in Fig. 6. In the first panel of Fig. 6a the surface reconstruction 'releases' the $O_{(3)}$ oxygens, thus facilitating their use in oxidizing the *para*-carbon of the ring; the latter is also seen to weaken its bonds with the neighboring *meta*-carbons, due to its diminished electron population. The other two $O_{(3)}$ sites, coordinated by the vanadium atom below the ring center, are seen to be more strongly bonded in the chemisorption system. When the distance between the adsorbate and substrate increases (Fig. 6b) all oxygen sites of the surface chemisorption region are more loosely bonded by the metal sites, the methyl C–H bonds are strengthened, while the ring electron population is diminished throughout most of its constituent atoms, particularly on the *meta*-hydrogens in the vicinity of the $O_{(1)}$ sites. These changes imply an increased tendency towards ring oxidation, particularly in the *meta*-position.

The next parallel arrangement (Fig. 6(c, d)) in the close approach complex generates some tendency towards the bond breaking on the methyl substituent (the forward $H \rightarrow O_{(2)}$ donation); one also detects in Fig. 6c the back donation from the four $O_{(3)}$ sites, all more tightly held by the vanadium atom, to the *ortho*- and *meta*-hydrogens in the ring. For the increased separation between reactants a stronger participation of the CT charge reorganization component and the reverse CT direction produce together a pattern in which the electrons are partially withdrawn from all constituent atoms in the ring, the methyl bonds are strengthened, and all nearby $O_{(2,3)}$ surface sites are more accessible (less tightly bonded to the vanadium atoms). This relative 'availability' of the lattice oxygens and a general tendency towards weakening of all bonds in the ring create favorable conditions for a nonselective ring oxidation (destruction).

Similar conclusions follow from the final pair of overall diagrams (Fig. 6(e, f)) for the third parallel arrangement. Namely, at the shorter separation the ring activation is more selective, due to the stronger P component, and the surface bridging oxygen sites coordinate more electrons to neighboring vanadium atoms and the methyl hydrogens; at the larger distance the CT component and the reverse CT direction create a delocalized pattern of bond weakenings in the

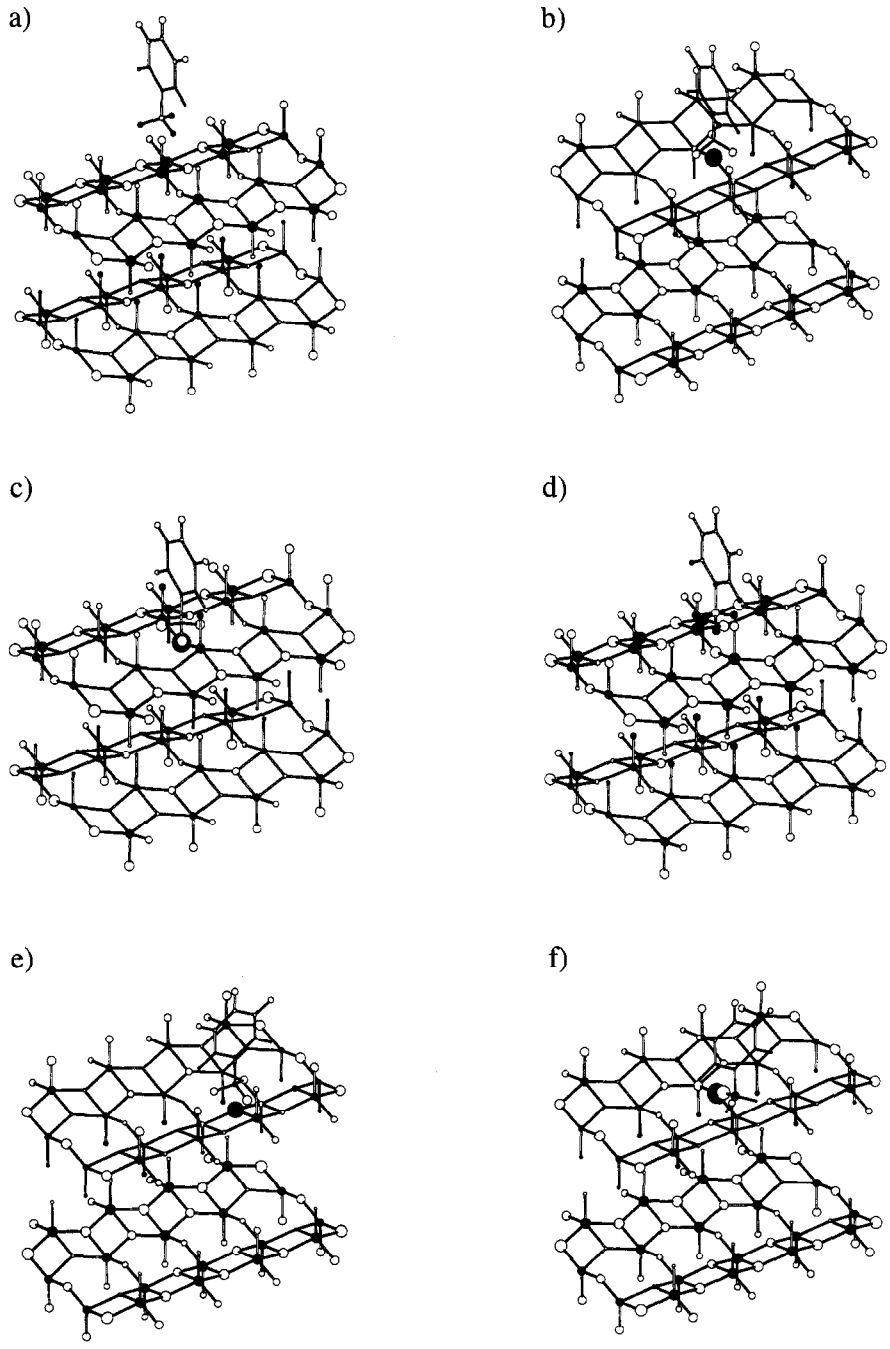

Fig. 7. The global (open system) FFI for the perpendicular chemisorption arrangements of Fig. 5.

ring, a strong lattice oxygens 'release', and a strengthening of the CH bonds in toluene. Hence, a selective oxidation at the *para*-carbon in the ring and on the methyl substituent is likely in the overall charge reorganization of Fig. 6e, while the nonselective ring oxidation (degradation) is more probable in the complex of Fig. 6f.

The energetical considerations (Eqs. (16a) and (16b)) indicate that the larger separations gener-

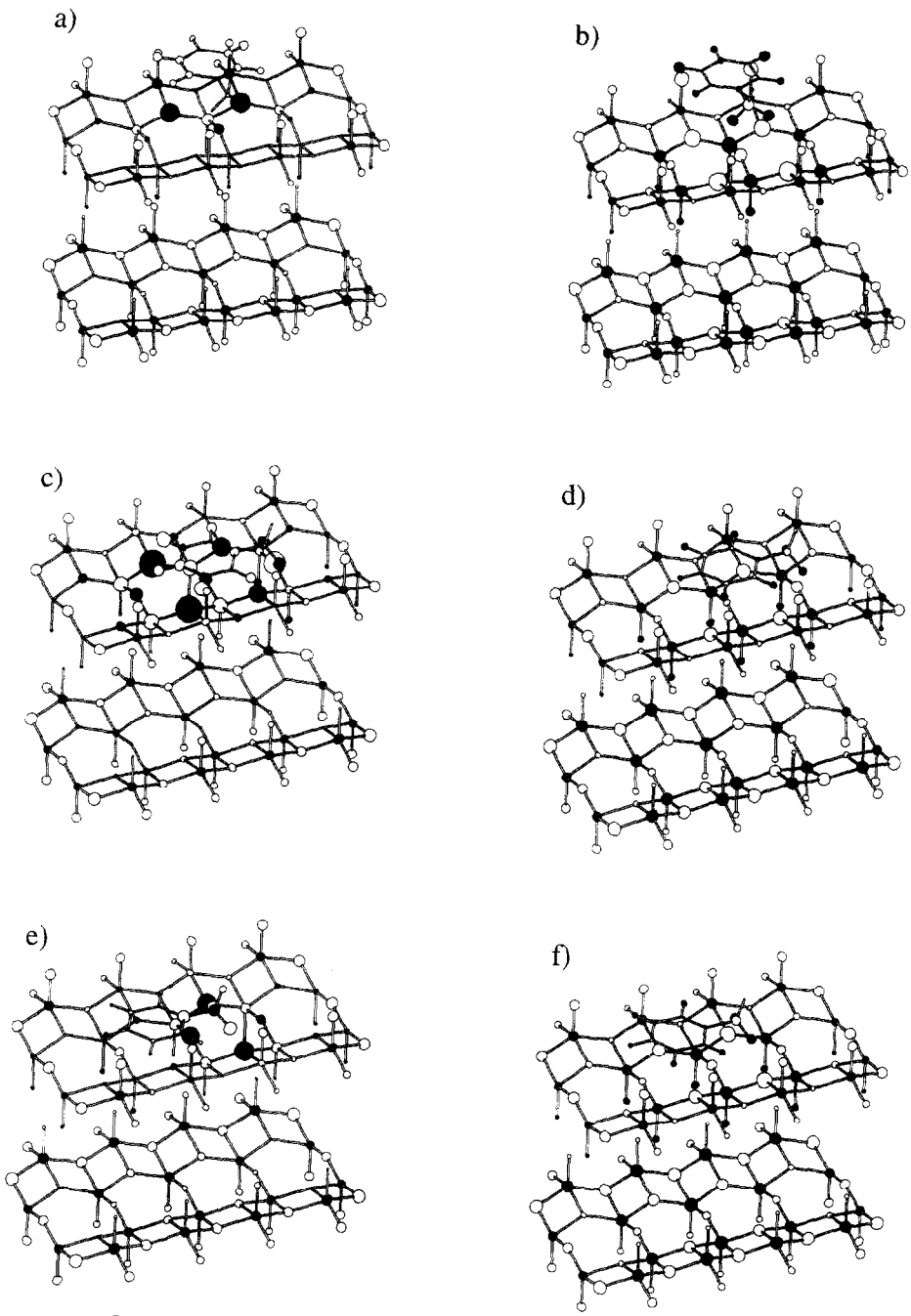

Fig. 8. The same as in Fig. 7 for the parallel chemisorption structures of Fig. 6.

ate larger stabilization energies; at this distance the overall pattern of charge displacements in benzene ring is practically nonselective. This strongly suggests that the parallel structures indeed promote the nonselective, total oxidation [13].

These general conclusions about the selective character of the toluene activation in the perpendicular complexes and the nonselective ring destruction in the parallel chemisorption arrangements qualitatively agree with the previously reported conjectures from the semiempirical calculations on selected toluene–$[V_2O_5]$ model systems involving very small non-stoichiometric clusters [13].

8. External charge transfer induced displacements

The global FFI for the chemisorption structures of Figs. 5 and 6 are shown in Figs. 7 and 8, respectively. They represent how an inflow of a single electron (a test, normalized chemical reduction of the system as a whole), from the external reservoir, redistributes itself in the system under consideration, when no constraints on the internal flows are imposed. These diagrams can therefore be used to probe the effect of an environmental CT upon the chemisorption, by comparing them with the respective isoelectronic CT patterns of Figs. 5 and 6. In systems, where the pattern of the in situ AIM displacements in the chemisorption region matches that observed in the global FFI diagrams, the overall system reduction ($dN > 0$) promotes the chemisorption (strengthens the adsorbate–substrate CT); similarly, in systems, where both these patterns exhibit opposite phases, the overall system oxidation ($dN < 0$) is required to promote the internal CT, i.e., the charge reorganization due to the $\mathcal{N}[dv]$ perturbation. In other words, a qualitative similarity between the isoelectronic and global CT patterns in the chemisorption region indicates that the system chemical oxidation hinders the inter-reactant CT and facilitates the associative (molecular) desorption of the adsorbate; the same chemisorption hampering influence of the overall chemical reduction is therefore predicted for the chemisorption systems, in which the respective CT/FFI patterns in the chemisorption region have opposite phases.

Such an overall similarity of the global FFI diagrams in the adsorption region to their isoelectronic analogs is detected in Fig. 7(a, b, d–f) and Fig. 8(a–f). In these systems $dN > 0$ promotes chemisorption (strengthens the chemisorption bond) and $dN < 0$ hinders the chemisorption (weakens the chemisorption bonds, promotes desorption). In Fig. 7c the trends exhibited by the main AIM displacements in the CH_3–$O_{(2)}$ region are opposite in the closed and open system cases, so that the above dN influences will be reversed in this particular complex.

Another general conclusion following from a comparison between the global and isoelectronic CT diagrams is that the latter are relatively localized and selective, probing mainly the region of a strong interreactant charge coupling. In the global FFI plots the inflowing charge generates AIM displacements throughout the system; the only exception to this delocalization feature of the global FFI diagrams is detected in Fig. 8c, where the chemisorption region exhibits increased amplitudes of the AIM charge shifts. Therefore, as already stressed elsewhere [2,3,5], the two reactant, in situ CT diagrams constitute much more subtle and selective diagnostic tools for probing $d\mathcal{N}$ reactivity trends, than the corresponding global FFI data of the reactive system as a whole.

9. Concluding remarks

The present calculations demonstrate that the inclusion of the external potential perturbation and all adsorbate–substrate charge couplings is necessary for an adequate probing of chemical reactivity trends in large systems, within a truly

two-reactant approach. The CSA in the AIM resolution provides a simple and efficient scheme for generating charge responses of interacting species, including both $d\mathbf{N}^{(+)}[d\mathbf{v}]_{\mathcal{N}=0}$ (P) and $d\mathbf{N}^{*}[\mathcal{N}]_{\mathbf{v}^0+d\mathbf{v}}$ (CT) components of the overall shifts in the AIM populations, $d\mathbf{N}[d\mathbf{v}, \mathcal{N}]$ (P + CT), due to the presence of the other reactant. This feature is particularly important for the heterogeneous catalysis since both the adsorbate activation and surface reconstruction trends can be quickly explored using these responses, before and after the interreactant CT. These three types of populational (charge) displacements in reactive systems have been demonstrated to constitute much more selective reactivity criteria than the global FFI of the chemisorption system as a whole. However, the latter allow one to additionally diagnose the effect of the external CT upon the adsorbate–substrate bond(s).

A remarkable localization of the isoelectronic charge responses in the catalytic systems, limited mainly to the chemisorption region, a posteriori validates the cluster approximation used in our analysis, since the responses in the missing crystal remainder can be safely extrapolated as marginal. In all cases the role of the supporting layer has been found to be relatively unimportant due to a relatively weak interlayer cherge coupling; only in the parallel adsorption arrangements, for short inter-reactant separations, it was predicted to be relatively more pronounced due to a stronger mutual perturbations of the adsorbate and substrate.

As a general rule, all the isoelectronic charge responses approximately represent the combined effect of the diagonal (direct) contribution of the adsorbate and the off-diagonal (induced) contribution of the substrate. The perpendicular adsorption diagrams consistently predict various degrees of the methyl bonds activation; only for one perpendicular complex a relatively strong influence upon the toluene ring is found. The parallel adsorption cases generate different patterns of the ring activation. It is found to be more specific (selective) for the close-approach structures, while the adsorption arrangements corresponding to larger inter-reactant separations facilitate a non-selective ring degradation. The charge displacement patterns predicted from the CSA calculations also reveal a strong surface reconstruction, often involving a 'disengagement' of the lattice oxygens, thus making them more accessible for oxidizing the adsorbate. These findings are in a qualitative agreement with the previous conclusions based upon the semi-empirical SCF MO calculations [13] for very small one layer clusters.

The present analysis also complements the recent probing of different reactivity trends in these systems using the minimum energy coordinates [1,12]. The latter examine how the local (AIM) test oxidations/reductions propagate themselves through the reactive system, under condition of the minimum energy. As such they adequately reflect the influence of the local (environmental), hypothetical manipulations on the reactive system and/or the effect of the reaction on one site upon the reactivity of another site in the system under consideration, e.g., the substituent effect.

A related two-reactant CSA study of the allyl-[MoO_3] chemisorption complexes will be published elsewhere [22].

Acknowledgements

This work was partly supported by a research grant from the Commission of European Communities (COST D3 and D5 Actions).

Appendix A. Charge response quantities expressed in terms of the AIM hardness matrix

The main purpose of this Appendix is to survey the expressions and/or algorithms for calculating all the charge response and related quantities discussed in this paper, from the canonical AIM chemical potentials and the hardness matrix grouping the second partial

derivatives with respect to AIM electron population variables:

$$\eta = (\partial^2 E/\partial \mathbf{N}\,\partial \mathbf{N})_{\mathbf{v}} = (\partial \mathbf{u}/\partial \mathbf{N})_{\mathbf{v}} = \{\eta_{i,j} \approx \gamma_{i,j}\}; \quad \text{(A.1)}$$

it can be realistically approximated via the corresponding valence-shell electron repulsion integrals $\{\gamma_{i,j}\}$ [1]; here $\mathbf{N} = (N_1, N_2, \ldots, N_m)$ and $\mathbf{u} = (\mu_1, \mu_2, \ldots, \mu_m)$ denote sets of the electron populations and chemical potentials (negative electronegativities, from the finite-differences) of the constituent AIM, respectively. The derivatives are calculated for the constant external potential due to the nuclei, $v(\mathbf{r}) = -Z_i/|\vec{r} - \vec{R}_i|$, in their fixed positions $\{\mathbf{R}_i \equiv \vec{R}_i\}$ (Born–Oppenheimer approximation), and Z_i stands for the nuclear atomic number. In this summary we shall follow the recent developments in the AIM-resolved CSA [2,3,5]. These canonical input quantities of the CSA in the AIM discretization consider the system energy as function of the AIM electron population and external potential variables, $\mathbf{v} = (v_1, v_2, \ldots, v_m)$: $E = E^{\mathrm{AIM}}(\mathbf{N}, \mathbf{v})$.

We consider a partitioning of the system $\mathrm{M} = (\mathrm{A}|\mathrm{B})$, consisting of two reactants A and B, e.g., the substrate and adsorbate in chemisorption systems. The system is therefore divided into mutually closed (but interacting) reactants. Let us denote the overall number of electrons in both subsystems by $N_{\mathrm{A}} = \sum_{\mathrm{a}}^{\mathrm{A}} N_{\mathrm{a}}$ and $N_{\mathrm{B}} = \sum_{\mathrm{b}}^{\mathrm{B}} N_{\mathrm{b}}$, where a and b denote constituent atoms of respective reactants, and $N_{\mathrm{A}} + N_{\mathrm{B}} = N$ is the global number of electrons in M. In such a reactant resolution the nonequilibrium system energy becomes the function of the separate AIM population vectors of both subsystems, $E = E^{(\mathrm{A}|\mathrm{B})}(\mathbf{N}_{\mathrm{A}}, \mathbf{N}_{\mathrm{B}}, \mathbf{v})$; this energy function depends only on global population variables in each reactant, $E = E_{\mathrm{eq}}^{(\mathrm{A}|\mathrm{B})}(N_{\mathrm{A}}, N_{\mathrm{B}}, \mathbf{v})$, at the equilibrium state $\mathrm{M}^{(+)} = (\mathrm{A}^{+}|\mathrm{B}^{+})$ in both mutually closed reactants. The constituent AIM of each subsystem are assumed to be in the equilibrium after the reactant mutual polarization, thus exhibiting the intra-reactant chemical potential/electronegativity equalization: $\mu_{\mathrm{X}}^{(+)}\mathbf{1}_{\mathrm{X}} = \mathbf{u}_{\mathrm{X}}^{\mathrm{eq}}$, X = A, B.

The relevant electronegativity equalization equations (EEE), which relate the intra-fragment charge rearrangements $\delta \mathbf{N}_{\mathrm{X}} = \mathbf{N}_{\mathrm{X}}^{(+)} - \mathbf{N}_{\mathrm{X}}^{0}$, X = A, B, leading to the equilibrium charge distributions $\mathbf{N}_{\mathrm{X}}^{(+)}$, from the initial (separated reactant) AIM electron populations $\mathbf{N}_{\mathrm{X}}^{0}$, can be written in the following matrix form:

$$\left[\mu_{\mathrm{A}}^{(+)}, \mu_{\mathrm{B}}^{(+)}, \delta \mathbf{N}_{\mathrm{A}}, \delta \mathbf{N}_{\mathrm{B}}\right] \times \begin{pmatrix} 0 & 0 & \mathbf{1}_{\mathrm{A}} & \mathbf{0}_{\mathrm{B}} \\ 0 & 0 & \mathbf{0}_{\mathrm{A}} & \mathbf{1}_{\mathrm{A}} \\ \mathbf{1}_{\mathrm{A}}^{\dagger} & \mathbf{0}_{\mathrm{B}}^{\dagger} & \eta^{\mathrm{A,A}} & \eta^{\mathrm{A,B}} \\ \mathbf{0}_{\mathrm{A}}^{\dagger} & \mathbf{1}_{\mathrm{B}}^{\dagger} & \eta^{\mathrm{B,A}} & \eta^{\mathrm{B,B}} \end{pmatrix} = \left[\mathrm{d}N_{\mathrm{A}}, \mathrm{d}N_{\mathrm{B}}, -\mathbf{u}_{\mathrm{A}}^{(+)}, -\mathbf{u}_{\mathrm{B}}^{(+)}\right]; \quad \text{(A.2)}$$

here the set $\{\eta^{\mathrm{X,Y}} \equiv (\partial \mathbf{u}_{\mathrm{Y}}/\partial \mathbf{N}_{\mathrm{X}})_{\mathbf{v}}\}$ represents the reactant resolved blocks in η, $\mathbf{u}_{\mathrm{A}}^{(+)} = \mu_{\mathrm{A}}^{0}\mathbf{1}_{\mathrm{A}} + \mathrm{d}\mathbf{v}_{\mathrm{A}}$ is the vector of the non-equalized AIM chemical potentials of the non-polarized ('frozen' AIM electron populations), closed reactants in the presence of each other, before the inter-reactant CT, and the vector $\mathrm{d}\mathbf{v}_{\mathrm{X}}$ groups electrostatic potentials (per electron charge) of the other reactant at positions of the constituent AIM in X: $\mathrm{d}\mathbf{v} = [\mathbf{v}_{\mathrm{B}}(\mathrm{A}), \mathbf{v}_{\mathrm{A}}(\mathrm{B})]$. In the present work the point-charge approximation to dv has been adopted:

$$\mathrm{d}\mathbf{v}_{\mathrm{A}} = \mathbf{v}_{\mathrm{B}}(\mathrm{A}) \cong -\sum_{\mathrm{b}}^{\mathrm{B}} q_{\mathrm{b}}/|\vec{R}_{\mathrm{a}} - \vec{R}_{\mathrm{b}}|,$$

$$\mathrm{d}\mathbf{v}_{\mathrm{B}} = \mathbf{v}_{\mathrm{A}}(\mathrm{B}) \cong -\sum_{\mathrm{a}}^{\mathrm{A}} q_{\mathrm{a}}/|\vec{R}_{\mathrm{a}} - \vec{R}_{\mathrm{b}}|, \quad \text{(A.3)}$$

where the net AIM charges $\{q_i = Z_i - N_i\}$.

Eq. (A.2), which can be written in short as: $\mathscr{R}(\mathrm{A}|\mathrm{B})\mathscr{H}(\mathrm{A}|\mathrm{B}) = \mathscr{P}(\mathrm{A}|\mathrm{B})$, determines generalized perturbations ('forces'), $\mathscr{P}(\mathrm{A}|\mathrm{B})$, from the generalized 'responses' $\mathscr{R}(\mathrm{A}|\mathrm{B})$ (negative displacements from the corresponding equilibrium values), with the latter being of the main interest in the theory of chemical reactivity. One

solves this equation for the response properties by inverting the generalized hardness matrix $\mathscr{H}(A|B)$, $\mathscr{R}(A|B) = \mathscr{P}(A|B)\mathscr{H}^{-1}(A|B) \equiv \mathscr{P}(A|B)\mathscr{S}(A|B)$:

$$\begin{aligned}&\left[-\mu_A^{(+)}, -\mu_B^{(+)}, \delta\mathbf{N}_A, \delta\mathbf{N}_B\right]\\ &\quad = \left[dN_A, dN_B, -\mathbf{u}_A^{(+)}, -\mathbf{u}_B^{(+)}\right]\\ &\begin{pmatrix} -\eta_{A,A} & -\eta_{A,B} & \mathbf{f}^{A,A} & \mathbf{f}^{A,B}\\ -\eta_{B,A} & -\eta_{B,B} & \mathbf{f}^{B,A} & \mathbf{f}^{B,B}\\ (\mathbf{f}^{A,A})^{\dagger} & (\mathbf{f}^{B,A})^{\dagger} & -\beta^{A,A} & -\beta^{A,B}\\ (\mathbf{f}^{A,B})^{\dagger} & (\mathbf{f}^{B,B})^{\dagger} & -\beta^{B,A} & -\beta^{B,B}\end{pmatrix}.\end{aligned} \tag{A.4}$$

The respective blocks in the generalized softness matrix $\mathscr{S}(A|B)$ in Eq. (A.4) are defined by the following derivatives:

(i) condensed chemical potentials and hardnesses:

$$\mu_X^{(+)} = \left[\partial E_{eq}^{(A|B)}/\partial N_X\right]_{\mathbf{v}}, \quad X = A, B; \tag{A.5a}$$

$$\eta_{X,Y} = \left[\partial^2 E_{eq}^{(A|B)}/\partial N_X \partial N_Y\right]_{\mathbf{v}} = \left(\partial\mu_Y^{(+)}/\partial N_X\right)_{\mathbf{v}} = \left(\partial\mu_X^{(+)}/\partial N_Y\right)_{\mathbf{v}}, \quad X = A, B; \tag{A.5b}$$

(ii) Fukui function indices (diagonal, X = Y, and off-diagonal, X ≠ Y):

$$\begin{aligned}\mathbf{f}^{X,Y} &= \left[\partial^2 E_{eq}^{(A|B)}/\partial\mathbf{v}_Y\,\partial N_X\right]_{N_Y,\mathbf{v}_X}\\ &= \left(\partial\mathbf{N}_Y/\partial N_X\right)_{\mathbf{N}_Y,\mathbf{v}}\\ &= \left(\partial\mu_X/\partial\mathbf{v}_Y\right)_{N_Y,N_Y,\mathbf{v}_X}, \quad X = A, B;\end{aligned} \tag{A.6}$$

(iii) reactant resolved blocks of the linear response matrix (diagonal, X = Y, and off-diagonal, X ≠ Y):

$$\begin{aligned}&\beta^{X,Y} = \left[\partial^2 E_{eq}^{(A|B)}/\partial\mathbf{v}_Y\partial\mathbf{v}_X\right]_{N_X,N_Y}\\ &\quad = \left(\partial\mathbf{N}_Y/\partial\mathbf{v}_X\right)_{\mathbf{N}_X,N_Y,\mathbf{v}_Y}, \quad X = A, B\\ &\quad \equiv \beta^{(A|B)}.\end{aligned} \tag{A.7}$$

The first two components of Eq. (A.4) determine the chemical potentials of the mutually closed, polarized reactants in contact with their separate particle reservoirs responsible for the allowed $dN_X \neq 0$ (X = A, B) degrees-of-freedom, while the remaining two sets of matrix equations determine the corresponding changes in the AIM electron populations. Clearly, when one considers the polarization of the externally and mutually closed reactants one puts $dN_X = 0$ (X = A, B) in the generalized perturbation vector $\mathscr{P}$.

When determining the global (g) equilibrium properties of M, one assumes that the mutually opened reactants have reached the global equilibrium state: $M^* = (A^*|B^*)$; in this resolution $E = E_g(N, \mathbf{v})$. The global analogs of Eqs. (A.2) and (A.4) are:

$$\begin{aligned}\left(-\mu^M, \delta\mathbf{N}\right)\begin{pmatrix} 0 & \mathbf{1}\\ \mathbf{1}^{\dagger} & \eta\end{pmatrix} &\equiv \mathscr{R}(A|B)\,\mathscr{H}(A|B)\\ &= (dN, -\mathbf{u}^{(+)})\\ &\equiv \mathscr{P}(A|B),\end{aligned} \tag{A.8}$$

$$\left(-\mu^M, \delta\mathbf{N}\right) = \mathscr{R}(A|B) = (dN, -\mathbf{u}^{(+)})\begin{pmatrix} -\eta^M & \mathbf{f}\\ \mathbf{f}^{\dagger} & -\beta\end{pmatrix} \equiv \mathscr{P}(A|B)\,\mathscr{S}(A|B). \tag{A.9}$$

In these two equations $\mu^M = (\partial E_g/\partial N)_{\mathbf{v}}$ is the system global chemical potential, $\mathbf{u}^{(+)} = (\mu_A^0\mathbf{1}_A + d\mathbf{v}_A, \mu_B^0\mathbf{1}_B + d\mathbf{v}_B)$ stands for the AIM chemical potentials of nonpolarized reactants, shifted by $d\mathbf{v}$ from the separated reactant values: $\mathbf{u}^0 = (\mu_A^0\mathbf{1}_A, \mu_B^0\mathbf{1}_B)$, where $\mu_A^0 = [\partial E_A(N_A, \mathbf{v}_A)/\partial N_A)_{\mathbf{v}_A^0}$, etc., $\eta^M = (\partial^2 E_g/\partial N^2)_{\mathbf{v}} = (\partial\mu^M/\partial N)_{\mathbf{v}} = S^{-1}$ denotes the global hardness of M, the inverse of its global softness S, and the global Fukui function indices represent the mixed derivatives of the system energy:

$$\begin{aligned}\mathbf{f} &= \left(\partial^2 E_g/\partial N\partial\mathbf{v}\right) = \left(\partial\mu^M/\partial\mathbf{v}\right)_N\\ &= \left(\partial\mathbf{N}/\partial N\right)_{\mathbf{v}}.\end{aligned} \tag{A.10}$$

The global chemical potentials of isolated reactants are obtained from separate global CSA calculations on each reactant, using the diagonal blocks $\{\eta^{X,X}\}$ as the system hardness matrices.

The separate reactant Fukui functions of Eq. (A.10), $\mathbf{f}^{X} = (\partial \mathbf{N}_X / \partial N_X)_{v_X}$, provide the weighing factors in the chain-rule formula expressing the reactant global chemical potentials in terms of the canonical AIM chemical potentials $\mathbf{u}^0 = (\partial \boldsymbol{E}_X / \partial \mathbf{N}_X)_{v_X} = \{\mu_x^0\}$:

$$\mu_X^0 = \sum_x^X f_x^X \mu_x^0, \quad X = A, B. \tag{A.11}$$

References

[1] R.F. Nalewajski, Struct. Bond. 80 (1993) 115; in: Proceedings of the NATO ASI on Density Functional Theory, Il Ciocco, August 16–27, 1993, E.K.U. Gross and R.M. Dreizler (Eds.) (Plenum Press, New York, 1995) p. 339; B.G. Baekelandt, W.J. Mortier and R.A. Schoonheydt, Struct. Bond. 80 (1993) 187.

[2] R.F. Nalewajski, J. Korchowiec and A. Michalak, in: Topics in Current Chemistry: Density Functional Theory of Chemical Reactivity, R.F. Nalewajski (Ed.) (Springer-Verlag, Heidelberg), 183 (1996) 25.

[3] R.F. Nalewajski and J. Korchowiec, Charge Sensitivity Approach to Molecular Structure and Chemical Reactivity (World Scientific, Singapore, 1996), in press.

[4] B.G. Baekelandt, G.O.A. Janssens, H. Toufar, W.J. Mortier, R.A. Schoonheydt and R.F. Nalewajski, J. Phys. Chem. 99 (1995) 9784.

[5] R.F. Nalewajski, Int. J. Quantum Chem. 56 (1995) 453; R.F. Nalewajski, Int. J. Quantum Chem., in press.

[6] R. Pariser, J. Chem. Phys. 21 (1953) 568; K. Ohno, Theor. Chim. Acta 10 (1968) 111; Adv. Quant. Chem. 4 (1967) 239.

[7] P. Hohenberg and W. Kohn, Phys. Rev. B 136 (1964) 864; W. Kohn and L.J. Sham, Phys. Rev. A 140 (1965) 1133.

[8] R.G. Parr and W. Yang, Density Functional Theory of Atoms and Molecules (Oxford University Press, New York, 1989), and references therein.

[9] R.M. Dreizler and E.K.U. Gross, Density Functional Theory: an Approach to the Quantum Many-Body Problem (Springer-Verlag, Heidelberg, 1990).

[10] R.F. Nalewajski, J. Korchowiec, R. Tokarz, E. Brocławik and M. Witko, J. Mol. Catal. 77 (1992) 165; R.F. Nalewajski and J. Korchowiec, J. Mol. Catal. 82 (1993) 383.

[11] R.F. Nalewajski, J. Korchowiec and A. Michalak, Proc. Indian Acad. Sci. (Chemical Sci.) 106 (1994) 353.

[12] R.F. Nalewajski and A. Michalak, Int. J. Quantum Chem. 56 (1995) 603.

[13] M. Witko, R. Tokarz and J. Haber, J. Mol. Catal. 66 (1991) 205, 357; M. Witko, J. Haber and R. Tokarz, J. Mol. Catal. 82 (1993) 457; J. Haber and M. Witko, Catal. Today, 23 (1995) 311.

[14] R.F. Nalewajski and J. Korchowiec, Computers Chem. 19 (1995) 217.

[15] A. Michalak and K. Hermann, unpublished results.

[16] O. Madelung (Ed.), Landolt–Börnstein: Numerical Data and Functional Relationships in Sciences and Technology: Crystal and Solid State Physics, Vol. 17: Semiconductors: (g) – Physics of Non-Tetrahedrally Bonded Binary Compounds III (Springer-Verlag, Heidelberg, 1984) p. 486.

[17] R.F. Nalewajski, Int. J. Quantum Chem. 49 (1994) 675.

[18] J. Korchowiec, H. Gerwens and K. Jug, Chem. Phys. Lett. 222 (1994) 58.

[19] D.N. Nanda and K. Jug, Theoret. Chim. Acta 57 (1980) 95; K. Jug, R. Iffert and J. Schulz, Int. J. Quantum Chem. 32 (1992) 265; K. Jug, J. Comput. Chem. 13 (1992) 85.

[20] A. Gołebiewski, R.F. Nalewajski and M. Witko, Acta Phys. Polon. A 51 (1977) 617; A. Gołebiewski, in: Theory-Structure Properties of Complex Compounds (Polish Scientific Publiers, Warsaw, 1979) p. 117, and references therein.

[21] J.P. Perdew, R.G. Parr, M. Levy and J.L. Balduz, Phys. Rev. Lett. 49 (1982) 1691.

[22] R.F. Nalewajski and A. Michalak, J. Phys. Chem., submitted for publication.